Performance Evaluation of Silicon Drift Detectors for a Precision Spectroscopy of Kaonic Helium-3 X-rays

K中間子ヘリウム3原子のX線精密分光実験に用いるシリコンドリフト検出器の性能評価

Tadashi Hashimoto
橋本 直

Department of Physics, School of Science
University of Tokyo

February 2011

Abstract

A new precise measurement of kaonic helium-3 x-rays is going to be performed as the first experiment at the K1.8BR beamline in the J-PARC hadron experimental facility. The experiment aims to determine the strong-interaction-induced 2p shift with a precision below 2 eV, which provides crucial information on the $\bar{K}$-nucleus strong interaction in the low energy limit.

For the detection of the $\sim$ 6.2 keV x-rays from the 3d $\rightarrow$ 2p transitions in kaonic helium-3, 8 silicon drift detectors (SDDs), which have good resolutions in both timing and energy, will be used.

The operation of the SDD was established under the experimentally required condition; SDDs at low temperatures and their preamplifiers also in the vacuum. In the optimized temperature conditions, the energy resolution was $\sim$150 eV in FWHM at 6 keV and the time resolution was $\sim$500 ns in FWHM. The operation under the realistic beam condition was also confirmed with a good energy resolution and a good signal-to-noise ratio.

Furthermore, The response function of the SDD was studied to minimize the systematic error in the fitting of the obtained spectrum. Pileup events were successfully removed and the effect of the different incident angle was investigated. The validity of the energy scale at 6 keV in our system was estimated to be better than 1 eV.

Contents

List of Figures

List of Tables

Chapter 1

Introduction

1.1 Kaonic Atom X-rays

Hadronic atoms reveal the effect of the strong interaction in terms of shifts and broadenings of their low-lying atomic states compared to the pure electromagnetic values. Experimentally, they can be produced by stopping negative hadrons such as π^-, $\bar{p}$, K^- , Σ^- in the target. The negative hadron is initially captured at highly excited state with a principal number $\sim \sqrt{\frac{M_X^*}{m_e}}$, where M_X^* denotes the reduced mass of the hadronic atom system, then deexcite by emitting Auger electrons and x-rays. The spectroscopy of the x-rays feeding "last orbit", where the hadron-nucleus strong-interaction width become larger than the radiative transition width, is therefore a unique tool to precisely determine the hadron-nucleus strong interaction in the low energy limit.

Although a wide range of pionic atom data with high precisions are available, the data of kaonic atom x-rays are poor in both quality and quantity mainly due to the lack of the intense kaon beam [1]. Especially, in light kaonic atoms with targets Z$\leq$2 , there were confusing "puzzles" in the past century and the precisions of the measurements are still not satisfactory.

1.2 History of Kaonic Helium X-ray Studies

First of all, the definition of the energy level shift (ΔE) in this thesis should be clarified. The shift is defined by

$$\Delta E = -(E^{strong} - E^{e.m.}), \tag{1.1}$$

where E^{strong} is a strong-interaction-affected (i.e. actual) energy level which can derive from measured x-ray energies and $E^{e.m.}$ is a calculated energy level assuming only the Coulomb interaction. In this definition, a positive ΔE means an attractive shift.

1.2.1 "Kaonic Helium Puzzle"

In the last century, three experiments observed kaonic ^{4}He 3d $\rightarrow$ 2p x-rays [2–4]. 2p level is the "last orbit" in the kaonic He atom. All of these experiments reported a relatively large repulsive 2p shift and a large width. Their average is

$$\Delta E_{2p}^{old} = -43 \pm 8\,\text{eV}, \qquad \Gamma_{2p}^{old} = 55 \pm 34\,\text{eV} \tag{1.2}$$

In contrast, optical model calculations result in very small shifts and widths [5, 6], for example [5],

$$\Delta E_{2p}^{opt} = 0.13 \pm 0.02\,\text{eV}, \qquad \Gamma_{2p}^{opt} = 1.8 \pm 0.05\,\text{eV} \tag{1.3}$$

The difference in the shifts between the experiments and the theory was as much as 5σ, and this situation was called the "kaonic helium puzzle".

1.2.2 Connection to "Kaonic Nuclear Bound States"

The atomic level shift become more attractive as the attractive interaction between $\bar{K}$-nucleus increases, until the interaction become sufficiently strong to confine the atomic wave function in the local potential. Then, the atomic wave function acquires a node in the nuclear surface, which pushes the atomic state to the repulsive side. [7, 8] (for example, Fig. 1.1).

Therefore, the observed repulsive shift in the kaonic ^{4}He 2p state can be interpreted as an evidence of the existence of p-wave kaon-nuclear bound state [9, 10]. But in the optical model, the observed large shift can be reproduced only when the imaginary part of the potential is much smaller than the value obtained from the global fit of kaonic atom data for Z≥3 [5].

In the late 1990's, the attractive $\bar{K}N$ strong interaction was established by the KpX experiment at KEK [11]. It motivated Akaishi and Yamazaki to predict an unconventionally deep phenomenological $\bar{K}$-nucleus potential which accommodates narrow deeply-bound kaonic nuclei. They treated the $\Lambda(1405)$ as a $\bar{K}N$ bound state and used g-matrix method [12]. Their framework was also applied to kaonic He atoms [13]. Akaishi used a coupled-channel potential to avoid the difficulty in the imaginary part of the optical potential, then he showed the 2p shift in Kaonic ^{4}He and ^{3}He can be $|\Delta E| \leq$ 11 and 15 eV, respectively, if $\bar{K}$-nucleus potentials are deep as Akaishi and Yamazaki predicted (Fig. 1.1).

Even though the much larger shifts in the experiment cannot be explained, "kaonic helium puzzle" attracted renewed interest.

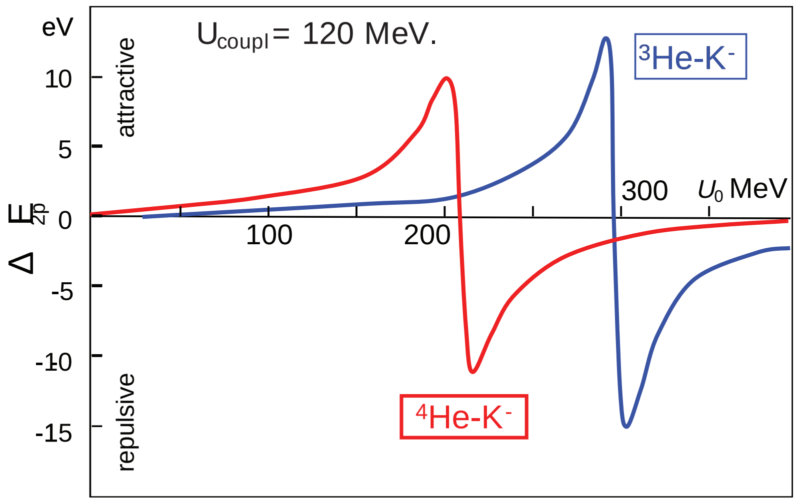

Figure 1.1: Akaishi's coupled-channel calculation for the 2p shifts in kaonic He atoms [13]

1.2.3 KEK-PS E570

The situation triggered to carry out a new high precision measurement of kaonic ^{4}He x-rays. KEK-PS E570 collaboration measured them, by using a liquid target and sophisticated techniques described in the following [14].

- High energy resolution using Silicon Drift Detectors (SDDs)
- Background suppression by a target volume cut with information of particle tracks
- In-beam absolute energy calibration

The detailed explanations of these techniques will appear in Sec 1.3 as we also employ them for the present kaonic ^{3}He experiment.

As a result, they achieved 2 times better resolution, 3 times higher statistics and 6 times better signal-to-noise ratio compared to the past experiments. Figure 1.2 shows the obtained spectrum in E570. The resulting 2p shift was

$$\Delta E_{2p}^{E570} = 2 \pm 2 \pm 2\,\mathrm{eV}, \tag{1.4}$$

which obviously differs from the previous experiments and is consistent to the theoretical calculations.

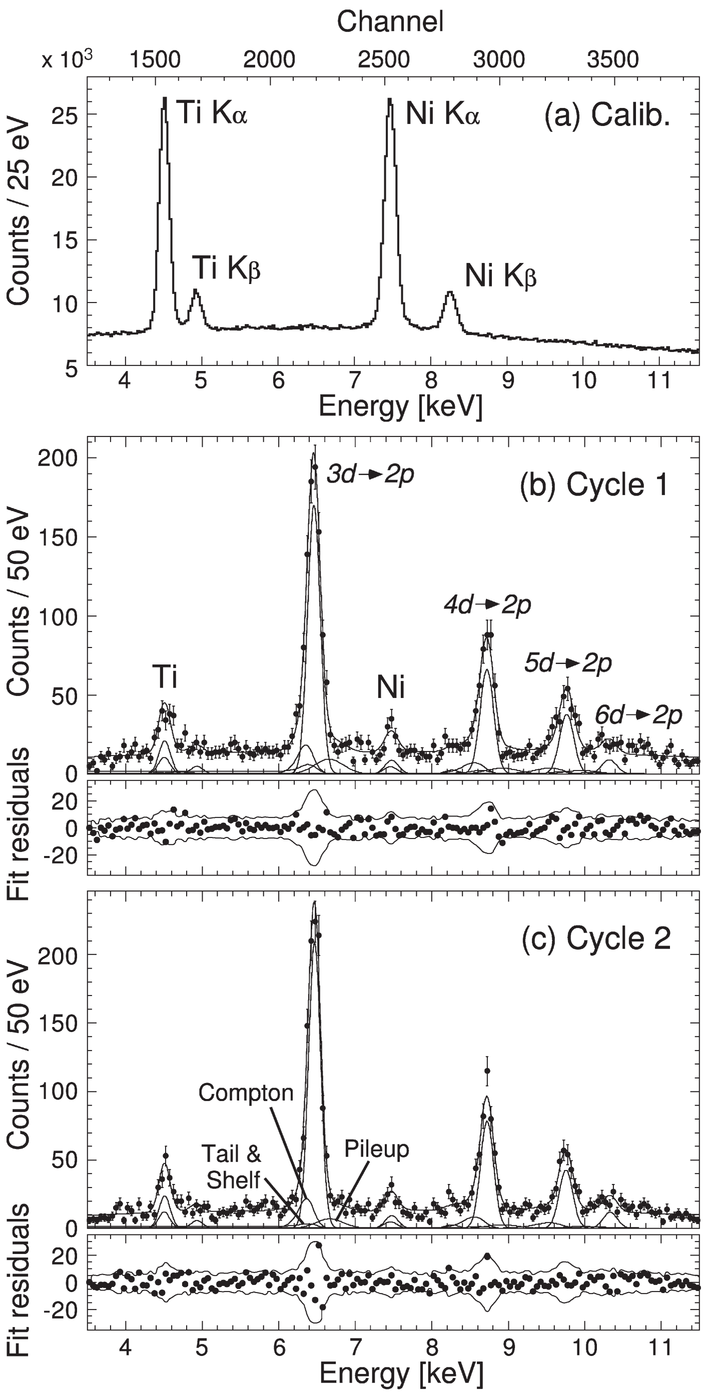

Figure 1.2: (a) Calibration spectrum (SDD self trigger) (b)(c) Kaonic ^{4}He spectra (stopped-K events) obtained in KEK-PS E570 [14].

1.2.4 SIDDHARTA Experiment

Soon after E570, another measurement on kaonic ^{4}He X-ray was reported by SIDDHARTA at DAΦNE, Italy [15]. The original purpose of SIDDHARTA is to precisely measure X-rays from kaonic hydrogen and deuterium. Since the x-ray energies of the 2p $\rightarrow$ 1s transitions in these atoms and the 3d $\rightarrow$ 2p transitions in both isotopes of kaonic helium atoms lies between 6 and 8 keV, they can also measure kaonic helium x-rays just replacing their target.

They effectively used gaseous target since the incident kaons from the ϕ decays are low momentum and almost mono energetic. 144 SDDs were arranged around the target and background was suppressed by using the SDD timing information. ^{55}Fe sources and titanium foils provided in-situ energy calibration in their case. The observed 2p shift in kaonic ^{4}He was

$$\Delta E_{2p}^{4He(test)} = 0 \pm 6 \pm 2\,\mathrm{eV}, \tag{1.5}$$

which confirmed the E570 result.

Very recently, the first measurement on kaonic ^{3}He was reported by SIDDHARTA together with a preliminary result of new kaonic ^{4}He data [16].

$$\begin{aligned} \Delta E_{2p}^{^3He} &= -2 \pm 2 \pm 4\,\mathrm{eV} & (1.6) \\ \Delta E_{2p}^{^4He(new)} &= 5 \pm 3 \pm 4\,\mathrm{eV}(preliminary) & (1.7) \end{aligned}$$

which are consistent with $\sim$ 0 eV shift. A large shift, initially seen in the kaonic ^{4}He 2p state, was not observed also in kaonic ^{3}He.

The experimental method was basically same as before except for the calibration method. This time, characteristic x-rays from titanium and copper foils induced by an x-ray tube provided the energy calibration. Note that the calibration data were obtained separately from the data taking of kaonic helium x-rays and at much higher intensity, which resulted in larger systematic errors. The obtained calibration spectra and kaonic ^{3}He spectrum are shown in Fig. 1.3 and Fig. 1.4.

It is worth mentioning that the difference between Eq. 1.6 and Eq. 1.7 is 7 eV $\pm$ 3.6 eV (stat.) which may be an indication of the finite isotope shift. Since these measurements were performed in the almost same condition, the isotope difference should be less affected by the systematic effects.

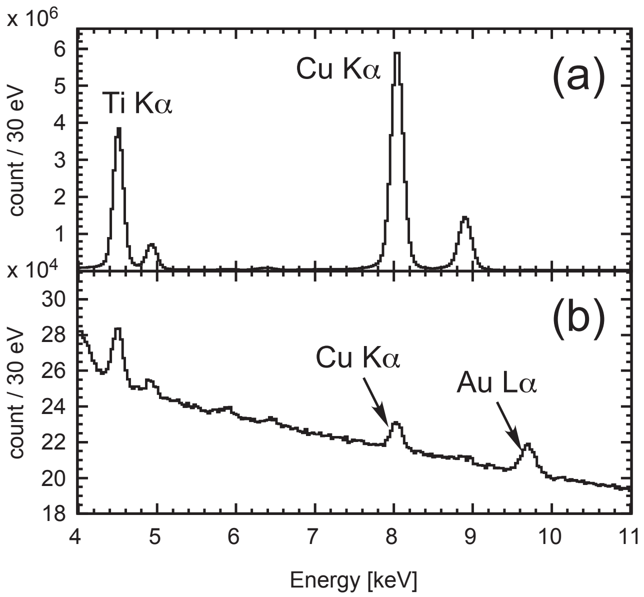

Figure 1.3: (a) A high statistics calibration spectrum with an x-ray tube (b) An in-beam spectrum without a kaon coincidence in the SIDDHARTA kaonic ^{3}He experiment. [16]

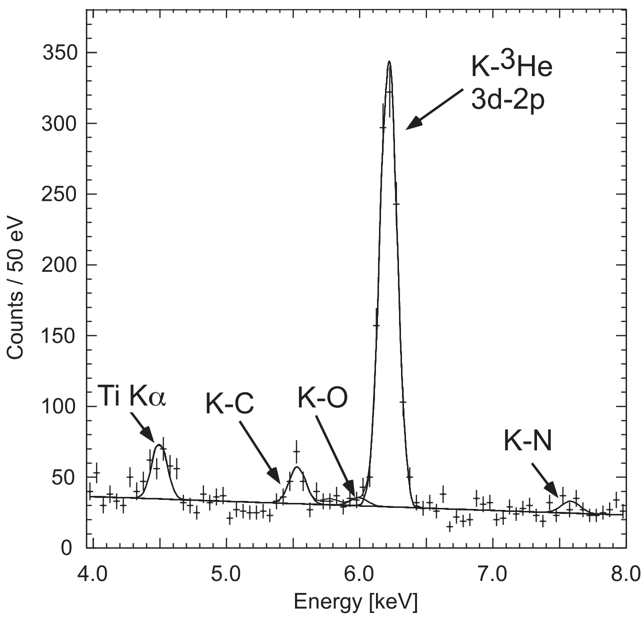

Figure 1.4: Kaonic ^{3}He spectrum (required a kaon coincidence) obtained in the SIDDHARTA experiment. [16]

All the results of the 2p shifts and widths in kaonic He obtained in the past experiments are plotted in Fig. 1.5 and Fig. 1.6, respectively. The error bars were defined by quadratic sum of the statistical error and systematic error.

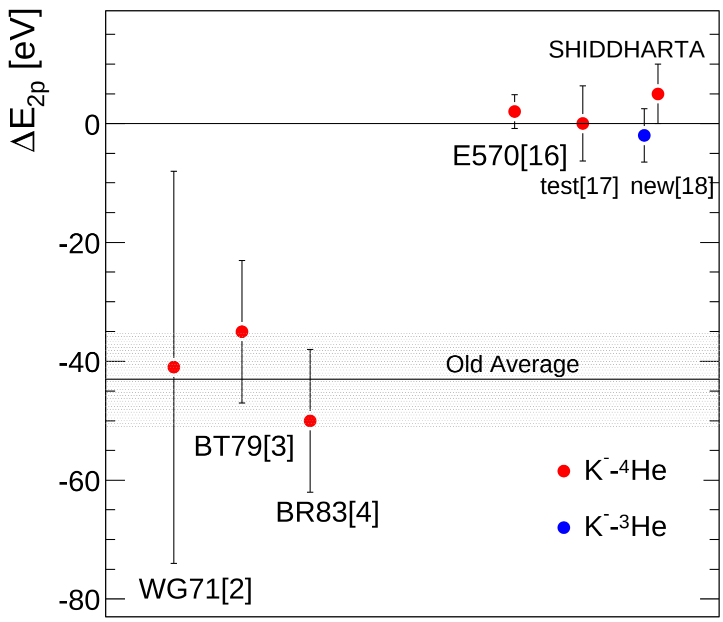

Figure 1.5: All the measured values of the 2p shifts in kaonic He atoms

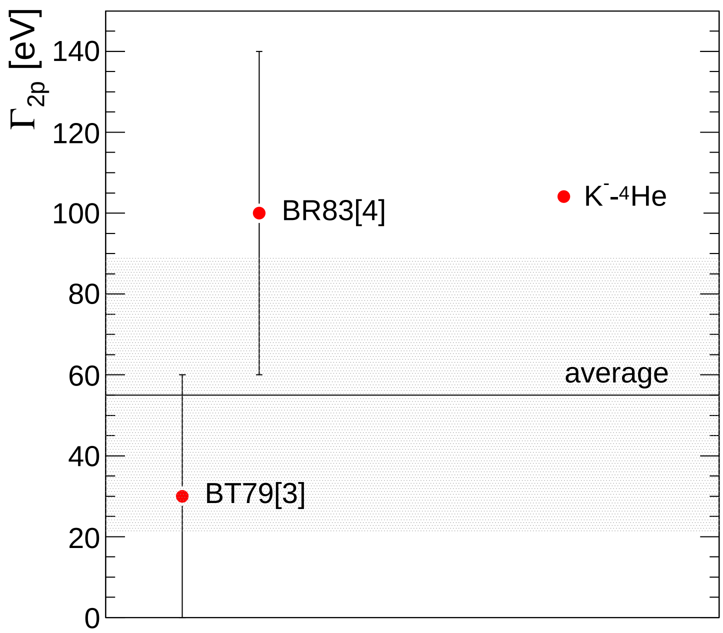

Figure 1.6: All the measured values of the 2p widths in kaonic He atoms

1.3 Present Experiment J-PARC E17

A new precision measurement of kaonic ^{3}He balmer series x-rays is going to be performed at J-PARC, Japan Proton Accelerator Research Complex. This experiment has been approved as E17 [17] and is the first experiment to be done at K1.8BR beamline in the Hadron Experimental Facility.

1.3.1 Experimental Strategy

Figure 1.7 shows the experimental setup. Incident kaons identified by the Lucite Cherenkov counters are degraded to stop inside the liquid-^{3}He target and resultant x-rays from the 3d $\rightarrow$ 2p transition in kaonic ^{3}He are measured by 8 Silicon Drift Detectors (SDD).

To determine the x-ray energy as precisely as possible, we use and refine the techniques which were successful in E570.

Silicon Drift Detectors (SDDs)

An SDD has a good time resolution of sub μs in addition to a good energy resolution $\sim$ 150 eV at 6.2 keV. It also have a thin active layer of 450 μm in spite of the 100 mm^2 large effective area, which reduces Compton background induced by high-energy γ-rays mainly from the π^0 and hyperon decays. The solid angle of 8 SDDs is $\sim$ 1 %.

Since a performance evaluation of SDDs is the main subject of this thesis, a detailed description of the detector will appear in the next chapter.

Background suppression by the target volume cut

Since the kaon is absorbed to nucleus after the atomic de-excitation and emit secondary charged particles, we can reconstruct reaction point by tracking both incident kaon and secondary charged particle. In E17, incident kaons are detected by the Small Drift Chamber (Small DC). Secondary charged particles are detected by the Cylindrical Detector System (CDS) which covers $\sim$ 60 % solid angle with a cylindrical drift chamber (CDC) and scintillation hodoscope counters (CDH). These detectors enables us to select x-rays originated only in the liquid ^{3}He target volume.

But in-flight decay or reaction events in the target cannot be rejected by the fiducial volume cut. Therefore, we additionally apply a correlation cut between the energy deposit on the E0 counters and the z-vertex position to reduce these events. As a result we can expect a good signal-to-noise ratio in the kaonic helium x-ray spectrum.

In-beam absolute energy calibration

An in-beam calibration is essential for this kind of precision measurement since it offsets various effects which come from the changes in the condition, such as a gain drift. In E17, characteristic x-rays from titanium and nickel foils, induced mainly by contaminating pions in the kaon beam, provide the in-situ and absolute energy calibration. The kaonic ^{3}He L_α line lies between the two K_α lines.

We will discuss validity of this calibration method in Sec 4.6.

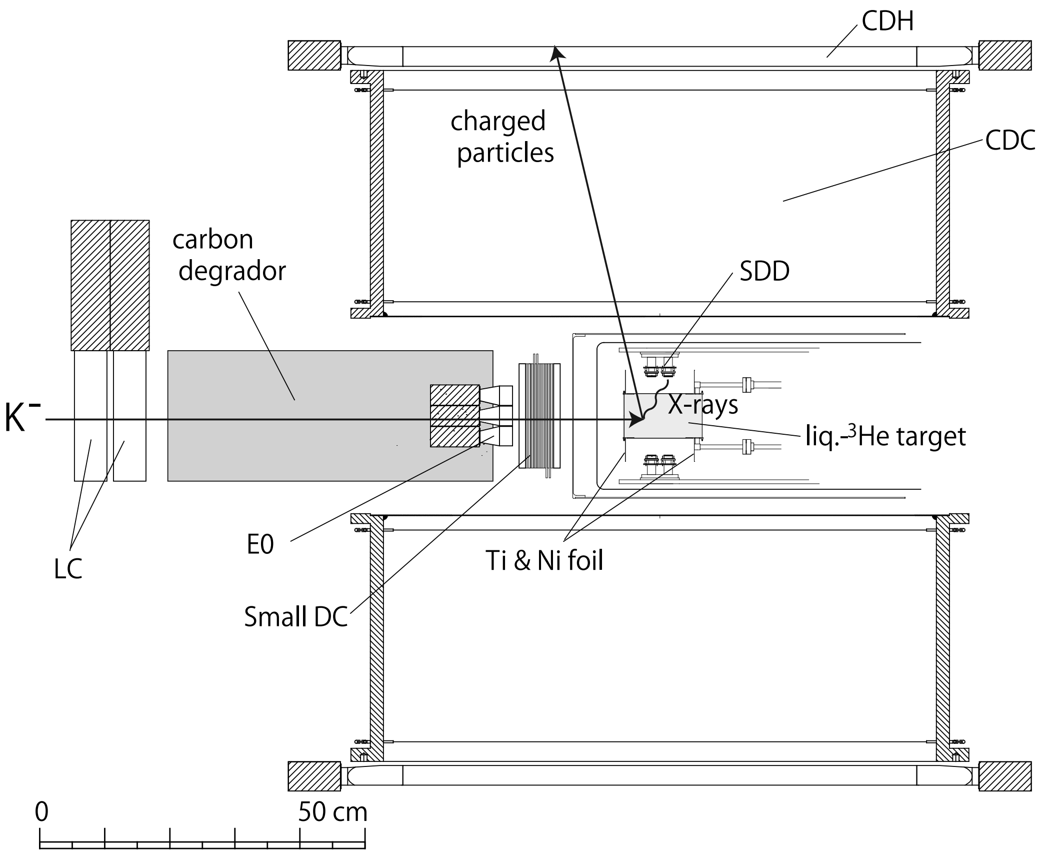

Figure 1.7: Experimental setup for E17

The pure-electromagnetic energy of the x-rays calculated in the framework of Klein-Gordon equation (K.G.) with the vacuum polarization effect (V.P.) from the first-order term of the Uehling potential are presented in Table 1.1.

Table 1.1: Calculated x-ray energy of the kaonic ^{3}He 3d $\rightarrow$ 2p transition [16]

Level	K.G. [eV]	V.P. [eV]	Total [eV]
2p	-11179.6	-15.4	-11195.0
3d	-4968.6	-1.9	-4970.5
3d $\rightarrow$ 2p	6211.0	13.5	6224.6

1.3.2 Precision Goal

Previous measurements of kaonic He x-rays were overviewed in the previous section. Although the long-standing "kaonic helium puzzle" has been solved, the precision is not satisfactory especially for kaonic ^{3}He and important questions still remain. They are

- Are the 2p shifts $\sim$ 0 eV or non-zero ($|\Delta E| > 2$ eV) ?
- Are the 2p shifts attractive or repulsive ?
- Is there a finite isotope shift?

These questions are essential to discuss the $\bar{K}$-nucleus interaction and the "kaonic nuclear bound state". Then, our precision goal in E17 is set to below 2 eV in both statistics and systematics and we aim to improve them up to 1 eV if possible. Since the detector resolution is $\sim$ 150 eV in FWHM, $\sim$ 1 eV seems to be the limit of the suppression of the systematic error. Furthermore, now we are thinking about re-measuring the kaonic ^{4}He x-rays in the same setup as the kaonic ^{3}He measurement to examine the indication of the finite isotope shift by the SIDDHARTA experiment.

Our precision goals are plotted with the results of recent measurements in Fig. 1.8.

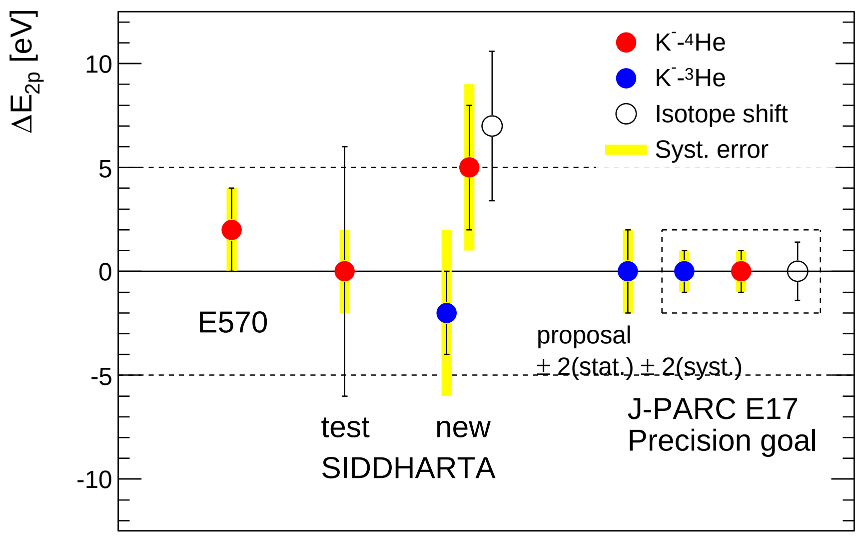

Figure 1.8: Recent measurements of the 2p shifts in kaonic He and our precision goal.

In addition to the precise determination of the 2p shift, information on the 2p width and the yields of x-rays are important. Therefore we will also determine these quantities. As for the 2p width, however, we may be able only to set a upper limit since the expected width is much smaller than the detector resolution.

Possible improvements from E570 for a better systematic error are as follows.

- Further optimization of operational conditions of SDDs (Chapter 3)
- Better understanding of response function of SDDs (Chapter 4)
- Wave form analysis with FADC data
- Beam information for the calibration x-rays with a second level trigger scheme

- Higher beam quality, especially in K^-/π^- ratio, which improves signal-to-noise ratio

Latter three points were tested and studied in the realistic beam condition and partially described in Chapter 5.

Chapter 2

Silicon Drift Detectors

2.1 Basic Concept

The basic concept of silicon drift detectors (SDD) was originally developed by Gatti and Rehak [18] based on the principle of sideward depletion; a large volume of high-resistivity n-type silicon is fully depleted by a small-sized n^+ ohmic substrate contact. If the p^+ junctions covering both surfaces are designed to produce an electric field parallel to the surface with proper reverse-bias voltages, all the electron induced by particle injection drift to the n^+ substrate contact acting as a collecting anode.

Although this mechanism was originally developed for a position sensitive detector by using the drift time information, we use SDDs specialized for x-ray spectroscopies [19].

In this case, one side of an SDD is made of uniform p^+ junction as a homogeneous radiation entrance window. In the opposite surface, concentric ring-shaped p^+ junction stripes are placed to produce electric field in the radial direction toward small n^+ ohmic substrate contact in the center, which acts as a collecting anode. A schematic view of the SDD configuration and the typical potential distribution produced by the reverse-bias voltages are show in Fig. 2.1 and Fig. 2.2.

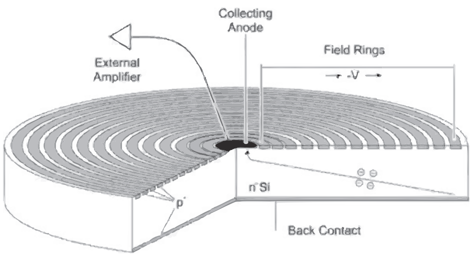

Figure 2.1: Schematic drawing of an SDD specialized for an x-ray measurement [19].

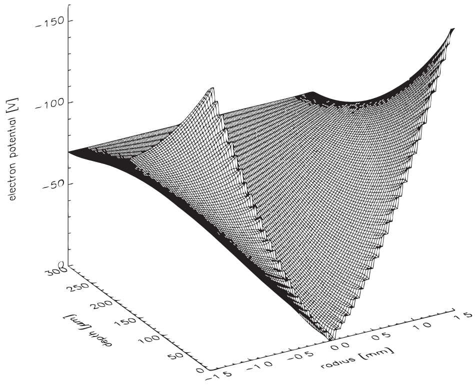

Figure 2.2: Typical potential distribution in an SDD [19].

As a result, an SDD can have a large effective area while keeping a small anode size and a thin active layer. The small anode size is vital for a good energy resolution and the thin active layer reduces the Compton background produced by high-energy γ-rays. The time resolution of an SDD reflects the drift time distribution of electrons in silicon, which is typically sub micro second at low temperatures.

They are now commercially available and we use SDDs and corresponding preamplifiers manufactured by KETEK [20].

Comparison with Previous Detectors

Here we compare the x-ray detectors used for x-ray spectroscopies of light kaonic atoms. A conventional Si(Li) detector cannot realize large effective area and thin active layer keeping a good energy resolution, whereas a charge coupled device (CCD) have no time resolution as summarized in Table 2.1. Thus, SDDs are the best devices among them for an x-ray spectroscopy of light kaonic atoms.

Table 2.1: Comparison of x-ray detectors used for kaonic x-ray measurements. KpX and DEAR were the experiments for kaonic hydrogen.

Detector	Si(Li)	CCD		SDD	
	KpX	DEAR	E570	Siddharta	E17
Effective area (mm^2)	200	724	100	100	100
Thickness (mm)	5	0.03	0.26	0.45	0.45
Energy resolution (FWHM) @ 6 keV (eV)	410	170	185	150	150
Temperature (K)	?	165	83	170	$\sim$130
Time resolution (FWHM) (ns)	290	-	430	690	$\sim$500
Reference	[11]	[21]	[14]	[22]	this thesis

2.2 Operational Requirement in E17

For a larger acceptance, SDDs are placed very close to the liquid-^{3}He target which will be held at $\sim$ 1.5 K. Therefore, low-temperature operation of SDDs are crucial to reduce thermal effect to the target. We put SDDs in a liquid-nitrogen cooled aluminum housing ($\sim$ 80 K) for this reason.

As for the preamplifiers, they should be placed close to the corresponding SDDs to minimize the cable lengths for the better resolution. Since our target cell, consequently SDDs are placed in the center of the cylindrical detector system, there is no space around the SDDs except for inside the target vacuum chamber. That's why we will operate the preamplifiers inside the vacuum unlike in the case of E570. They will be also placed inside a box cooled with liquid nitrogen.

Chapter 3

Optimization of Operational Conditions

As will be described in the chapters to follow, we performed various studies with 9 SDDs and 10 preamplifiers. Among them, 2 SDDs come from a different manufacturing lot and somehow showed different behavior for the bias-voltage. We distinguish them as “old” SDDs against other 7 “new” SDDs according to the order of purchases. 10 preamplifiers are considered to be basically identical. Table 3.1 shows the numbering of SDDs and preamplifiers.

The studies were performed at KEK (High Energy Accelerator Research Organization) and later at the J-PARC hadron experimental facility.

Table 3.1: Numbering of SDDs and preamplifiers

	Number	Remark
SDD	$1 \sim 6$, 9	“new”
	7, 8	“old”
Preamplifier	$1 \sim 10$	

3.1 Measurement Setup

To study the operational conditions of SDDs and other systematic effects, so-called test cryostat was prepared. It can provide the temperature conditions for SDDs and their preamplifiers described in the previous chapter with a much easier operation than the real experimental cryostat.

3.1.1 Test Cryostat

A schematic view of the test cryostat is shown in Fig. 3.1. The test cryostat was evacuated with a rotary pump and a turbo-molecular pump (TMP) to realize a thermal insulation vacuum. Then, liquid nitrogen was transferred to the 8 L tank. A copper support and a copper finger, which were directly connected to the liquid-nitrogen tank, were cooled down to below 80 K. An SDD and a preamplifier were mounted on the copper finger and the copper support, respectively. The SDD was irradiated to the x-rays from outside the vacuum through a 188 μm Mylar window (changed to 250 μm later).

A typical vacuum pressure with liquid-nitrogen cooling was of the order of 10^{-6} torr and a typical consumption time of fully-filled liquid nitrogen in the 8 L tank was around 14 hours.

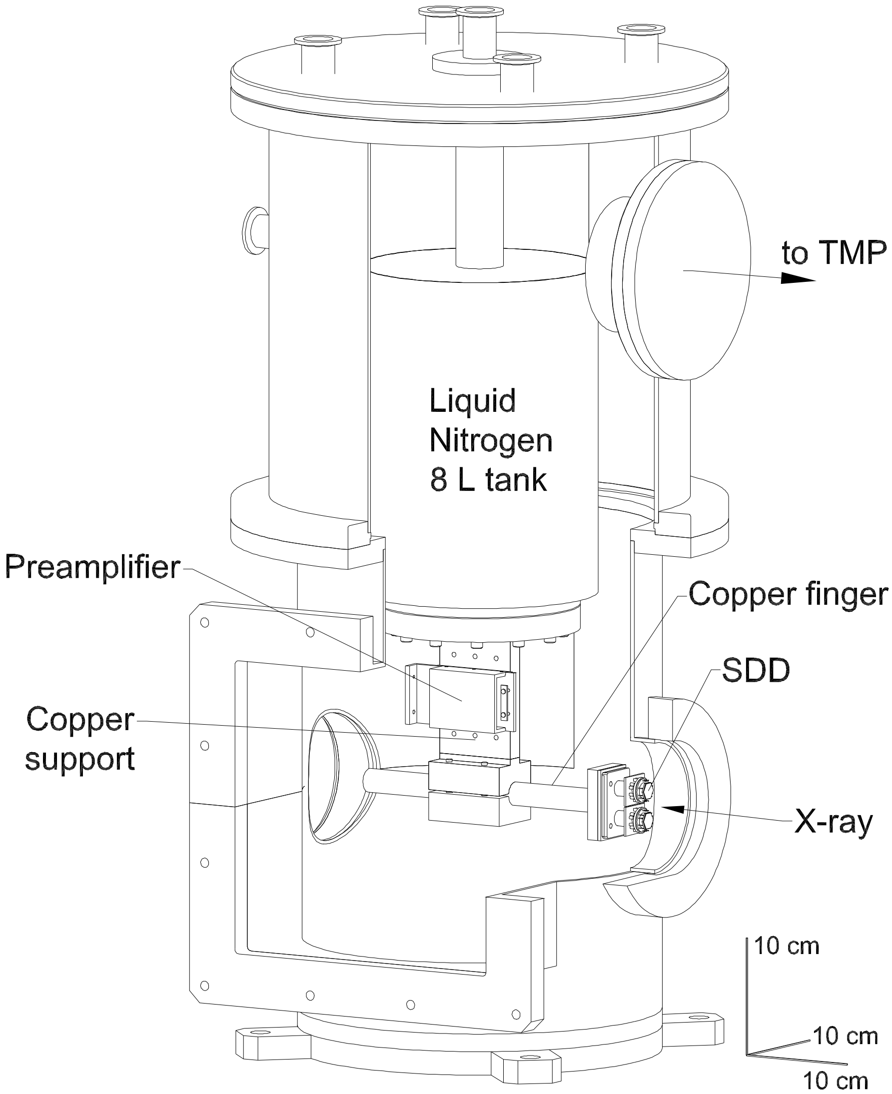

Figure 3.1: Schematic drawing of the test cryostat

3.1.2 PIPS Detector

For a timing measurement, we used a PIPS detector (passivated implemented planar silicon detector, manufactured by Canberra [23]) as a start counter. Even low energetic electrons from a ^{90}Sr source can easily penetrate the PIPS for its thinness of 300 μm. The time resolution of the PIPS detector was measured by using ^{90}Sr electrons and a scintillation counter to be $\sim$ 50 ns in FWHM.

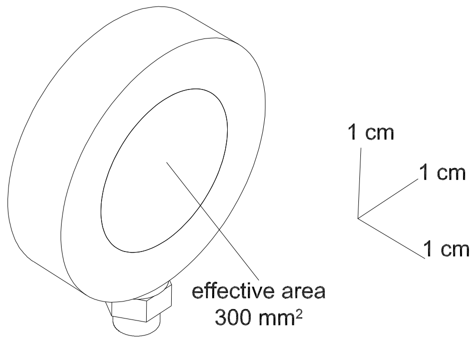

Figure 3.2: PIPS detector

3.1.3 Signal Readout

A schematic diagram of the signal flow from the SDD is shown in Fig. 3.3. High voltages supplied by KIKUSUI was divided to 3 voltages for R1 (most inner ring), RX (most outer ring), BACK (back contact) of an SDD(see Fig. 2.1). These bias voltages fully deplete the silicon bulk and make potential like Fig 2.2. For a preamplifier +12 V/ -12 V were supplied by an external voltage supplier.

A detected charge pulse was integrated by the reset-type charge-sensitive preamplifier separated by $\sim$ 40 cm from an SDD. Then, the ramped signal was taken out from the vacuum chamber and divided into two lines to input to a CAEN N568B shaping amplifier, where the signal was amplified and shaped. The preamplifier also generates so-called reset signal just after the reset timing.

The CAEN shaping amplifier has 16 channel inputs and 3 types of outputs for each 16 channel input. The features of these outputs are summarized in Table 3.2. We used 2 channels for each SDD. One of the outputs was negative with a 0.2 μs shaping time which was used for the trigger logic and the other one was positive output with 3 mus shaping time for a peak-hight measurement.

The CAEN N568B was also used for the PIPS detector.

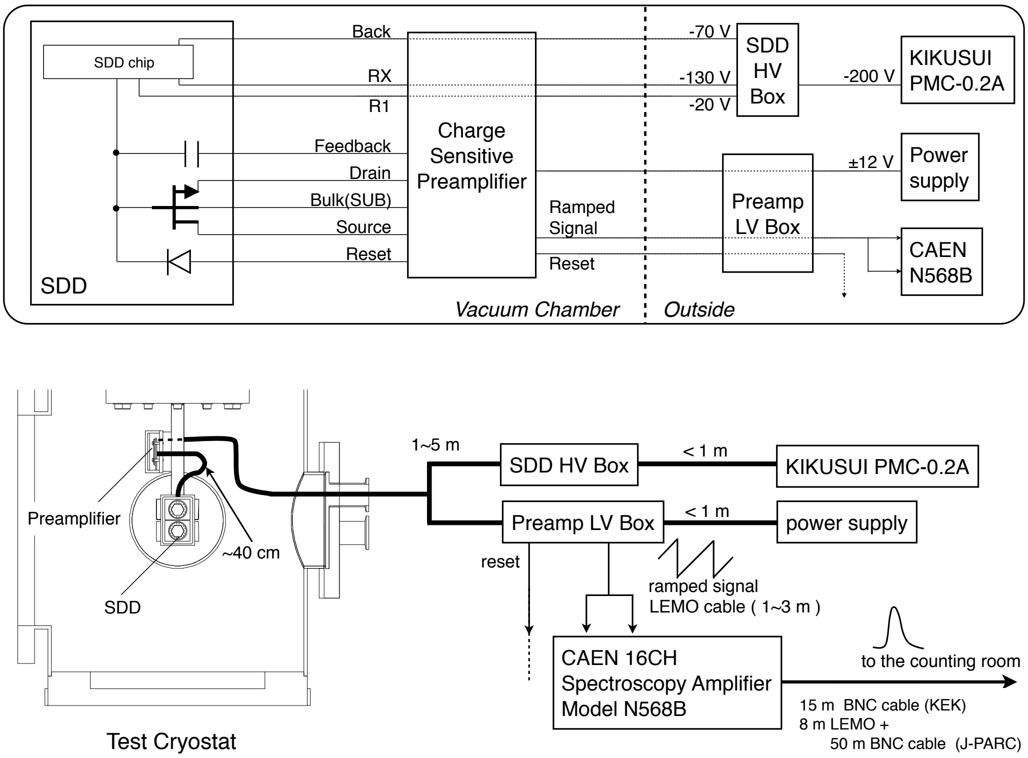

Figure 3.3: Flow of the SDD signal.

Table 3.2: Specifications of CAEN N568B shaping amplifier outputs

Name	Description
OUT	shaping time (0.2/1.0/3.0/6.0 μs) and polarity selectable
XOUT	further 10x fixed amplification of the OUT value
FOUT	100 ns differentiation time constant. Risetime: 25 ns typically.

3.1.4 Trigger Logic and Data Acquisition

At the very beginning of our study, we defined the trigger as (Figure 3.4 (a))

$$SDD \otimes \overline{Reset}.$$

Since the reset sometimes made fake signals and the baseline of the signal became unstable after a reset , $\overline{Reset}$ was introduced with a typical width of several hundreds μs.

In the timing measurement, a hit on PIPS detector was additionally required(Figure 3.4 (b)).

$$SDD \otimes \overline{Reset} \otimes PIPS,$$

where we selected only rapid rising signal for $PIPS$ by using a narrow coincidence window for two discriminators with different thresholds.

For the x-ray measurements with ^{90}Sr electron background, we used another discriminator and rejected large signals produced by electron direct hits.(Figure 3.4 (c))

$$SDD \otimes \overline{Reset} \otimes \overline{HighTh}$$

The pulse data (height/charge) of the signals and various timing information were fed into the PHADC, CHADC and TDC modules of the TKO standard. Then, they were read from VME-SMP via TKO SCH to record on the PC. The recorded signals in each measurement are summarized in Table 3.3.

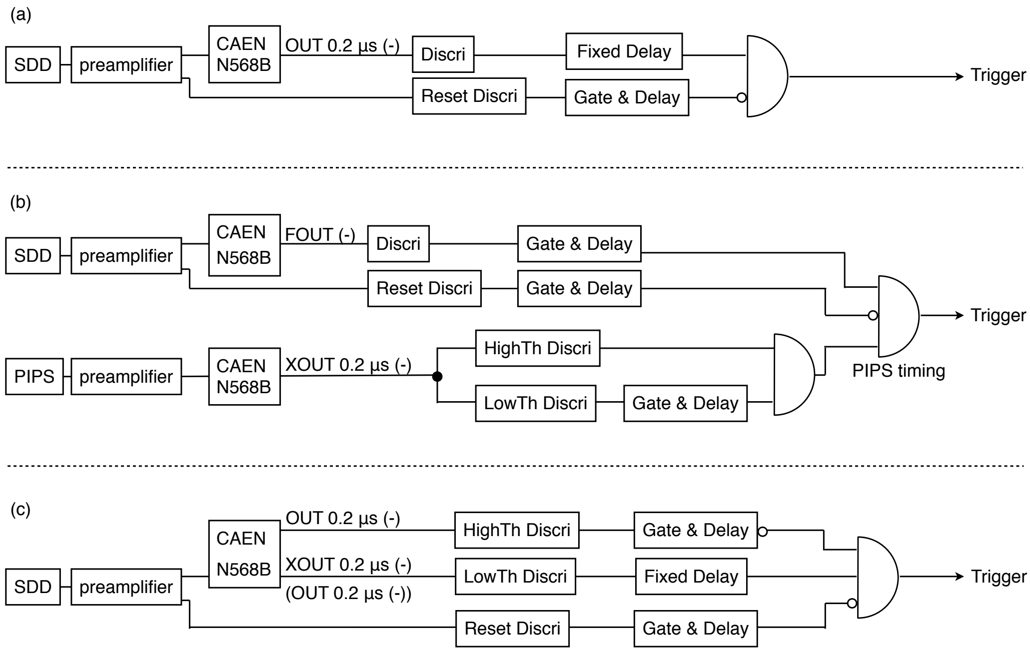

Figure 3.4: Trigger logics for the measurements at the test cryostat.

Table 3.3: Obtained data in the test cryostat measurements. ($*$) data were partially available.

	Name	Sh. Amp	(μs)	polality	module	remark
(a)	SDD ADC	OUT	3.0	positive	PHADC	
(b)	SDD ADC	OUT	3.0	positive	PHADC	
	SDD Timing	FOUT	-	negative	TDC (5 μs)	PIPS HighTh start
	PIPS ADC	XOUT	3.0	positive	PHADC	
	PIPS LowTh Timing	XOUT	0.2	negative	TDC (100 ns)	PIPS HighTh start
(c)	SDD ADC	OUT	3.0	positive	PHADC	
	Baseline	XOUT	3.0	positive	PHADC	$\sim$ 3.0 μs delay
$*$	FOUT	FOUT	-	positive	PHADC	$\sim$ 800 ns delay
$*$	Reset Timing	-	-	-	TDC (5 μs)	
$*$	Next Timing	OUT	0.2	negative	TDC (5 μs)	Discri V_{th}=30 mV
$*$	Tail Charge	OUT	0.2	negative	CHADC	

3.1.5 X-ray Sources

As an x-ray source, an ^{55}Fe is suitable in our case since the manganese x-ray lines are close to kaonic ^{3}He Lα line. Thus, an ^{55}Fe was used for various studies of the response of SDDs . A ^{90}Sr was used for the timing measurement and to obtain calibration lines of nickel and titanium fluorescence x-rays. The reference energies of these characteristic x-rays are listed in Table 3.4. Fe x-rays were used only in the beam commissioning (Chapter 5).

Table 3.4: Energies of characteristic x-rays used for the present study [24].

Metal	X-ray name	Energy (eV)
Ti	$K_{\alpha1}$	4510.90
	$K_{\alpha2}$	4504.92
	$K_{\beta1}$	4931.83
Mn (^{55}Fe)	$K_{\alpha1}$	5898.80
	$K_{\alpha2}$	5887.69
	$K_{\beta1}$	6490.59
Fe	$K_{\alpha1}$	6404.01
	$K_{\alpha2}$	6391.03
	$K_{\beta1}$	7058.18
Ni	$K_{\alpha1}$	7478.25
	$K_{\alpha2}$	7461.03
	$K_{\beta1}$	8264.78

3.2 Temperature Control

3.2.1 SDD Temperature Control

As mentioned above, SDDs were placed inside housings cooled down to liquid nitrogen temperature. But, SDDs themselves should be a bit warmed up as studies described in this section revealed.

Figure 3.5 shows the close-up drawing around the SDDs. Thermal contact between the base of the SDD housing and a SDD rod was reduced by a SUS bolt and a Teflon washer. Then, a film-type heater (120 Ω) attached on the rod could heat up a minimal region including the SDD itself when a

DC voltage was applied. A temperature sensor (LakeShore Pt-100) was also mounted on the rod and the temperature of the rod was defined as the SDD temperature.

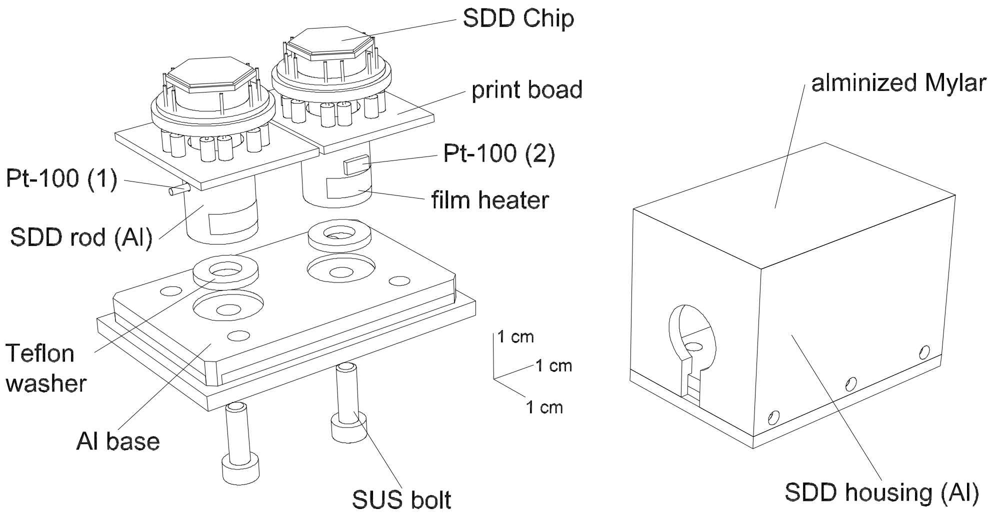

Figure 3.5: Close-up view around SDDs. As for the temperature sensors, two types of Pt-100s were used.

3.2.2 Preamplifier Temperature Control

Although we succeeded in operating our preamplifiers in the vacuum, one preamplifier was broken in the low-temperature operation at $\sim$ 150 K. We therefore decided to operate preamplifiers at the temperature over 200K to avoid such trouble although the direct cause of the breakdown was not clear.

A circuit board of a preamplifier was set in a housing with materials which optimize the heat conductance (Figure 3.6). An aluminum support for the preamplifier housing equipped a heater and a temperature sensor for the temperature control and mounted on the cold copper support with Teflon washers to reduce heat conductance. The temperature was controlled with a PID (Proportional-Integral-Derivative) feedback unit (Lakeshore 340). Another temperature sensor was attached on one of the chips of the preamplifier, whose temperature was adopted as the temperature of the preamplifier.

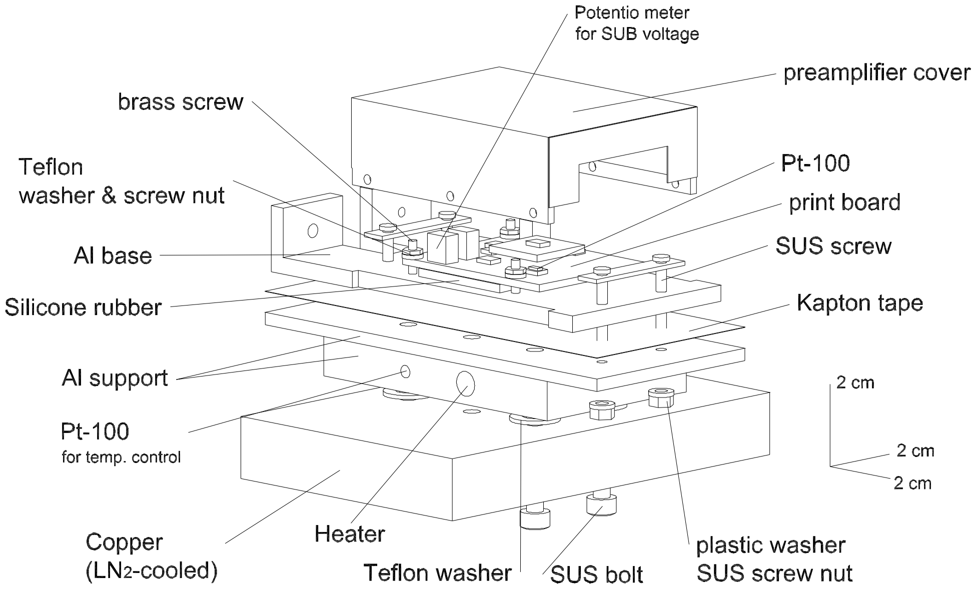

Figure 3.6: Close-up view around a preamplifier.

3.3 Optimization of Bias and Substrate Voltages

After roughly optimized operational temperatures of SDDs and their preamplifiers, optimal values of the bias voltages and the substrate voltage (SUB) of the FET were studied. We scanned around the values recommended by KETEK for R1/RX/BACK (-20V/-130V/-60V). Since we had to change SUB by the potentiometer on the preamplifier, we took out the preamplifier outside the vacuum for the SUB measurement.

As for R1 and RX, the recommended values were located in the stable regions. However, we found that the gain became smaller and resolution got worse just below the recommended value for BACK for “new” SDDs. Thus we adopted higher voltages for BACK. Although difference between “new” and “old” SDDs appeared in the behavior for the BACK voltage, they can share the same optimal voltages including the SUB voltage.

The results are shown in Fig. 3.7 together with arrows which indicate the adopted values. The energy resolutions were obtained by the fitting of ^{55}Fe spectra. The adopted voltages are summarized in Table 3.5 and a typical spectrum is shown in Fig. 3.8.

Although there were some differences in energy resolutions among SDDs, they were not characteristics of the detectors. The noise level usually changed when we open the cryostat for some modifications.

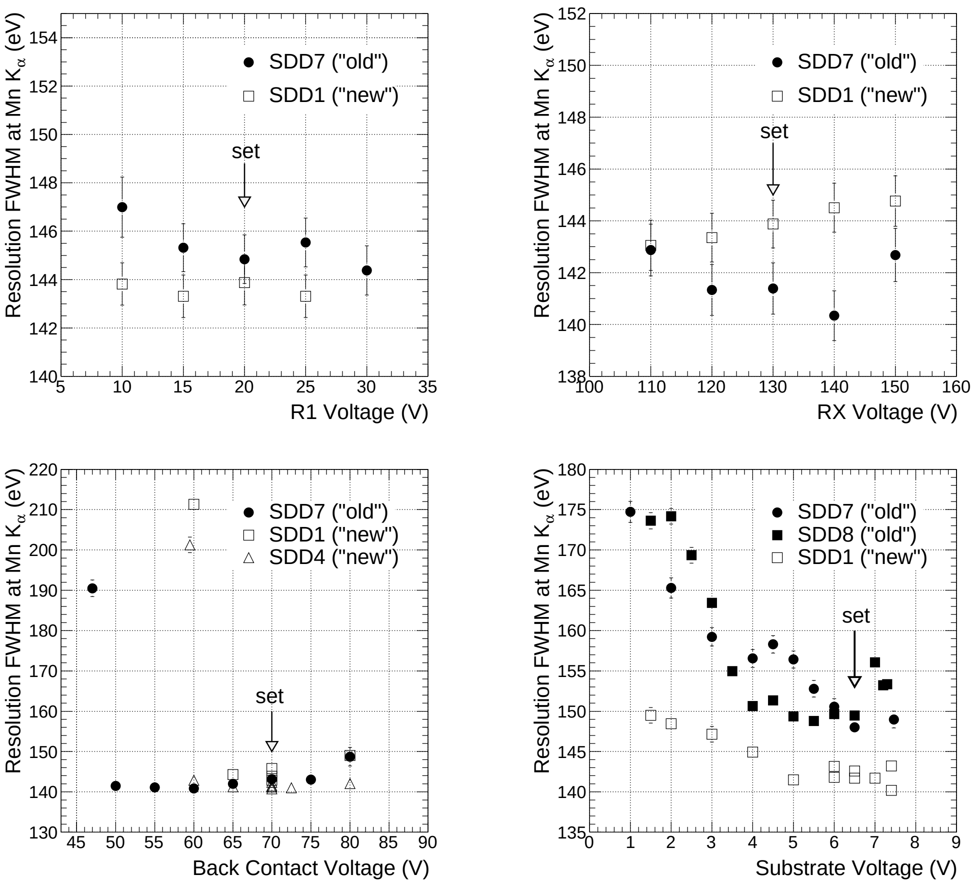

Figure 3.7: Results of the scans of bias voltages and a substrate voltage. The voltages except for the objective one were fixed to the optimized values.

Table 3.5: Optimized values for the bias and the substrate voltages

R1	RX	BACK	SUB
-20 V	-130 V	-70 V	-6.5 V

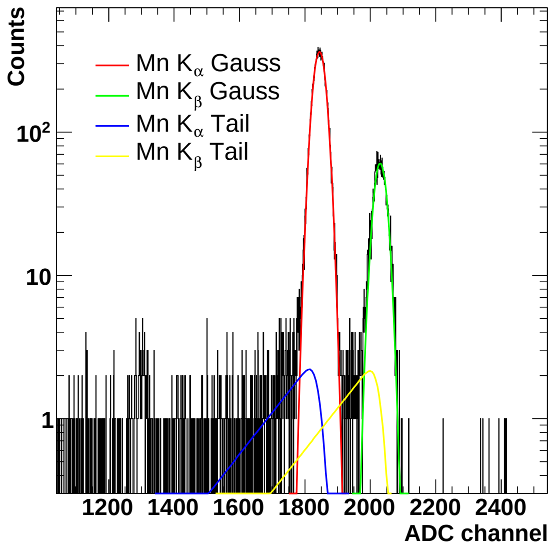

Figure 3.8: Typical ^{55}Fe spectrum obtained in the measurements for the optimization of the voltages. Only *Gauss* and *Tail* were used for the fitting (see Sec. 4.1).

3.4 Optimal Temperature Search

Now that optimal voltages were found, we systematically studied the optimal operational temperatures for preamplifiers and SDDs.

3.4.1 Preamp Temperature

At temperatures between 240 K and 290 K, we found energy resolutions are stable and Mn K_α peak positions moves 0.5 eV equivalent every 1 K change (Fig. 3.9). This peak shift is not so a large problem because the in-situ energy calibration compensates it in E17. Nevertheless, it is better to operate preamplifiers with stable temperatures.

The most severe constraint on preamplifiers' temperatures are related to the $\overline{Reset}$ veto time. The discharging time accompanied by reset has negative correlation on preamp temperature. When the discharging time becomes sufficiently longer, a large bump appears after reset in the shaped signal, which made us $\overline{Reset}$ veto time considerably long (an order of ms or more). To avoid such a long veto time, preamplifiers should be kept at > 270 K including some safety margin.

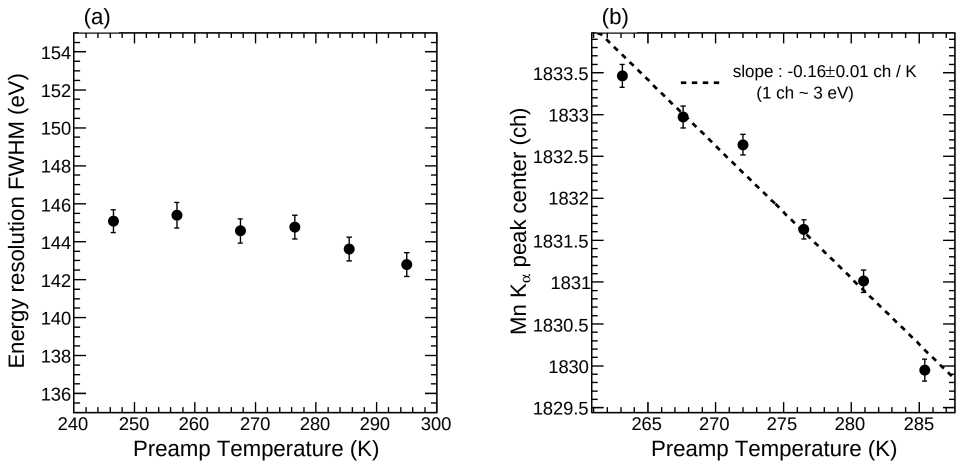

Figure 3.9: Preamplifier temperature dependence of (a) the energy resolution at Mn K_α (b) Mn K_α peak position

3.4.2 SDD Temperature

Time Resolution Measurement

Timing difference between electron hit on a PIPS and a penetrated electron hit on an SDD were measured to derive the time resolution of an SDD. A slewing effect of PIPS was corrected using parameters obtained in a measurement with a scintillation counter. Then, the slewing of SDD was corrected (Fig 3.10 (a)). After cutting off low signals, a timing histogram was fitted with a Gaussian and the time resolution of an SDD (ΔE_{SDD}) was defined as

$$\Delta E_{SDD} = 2\sqrt{2 \ln 2} \times \sigma_{Gaus}$$

where σ_{Gaus} is the Gaussian sigma obtained in the fitting.

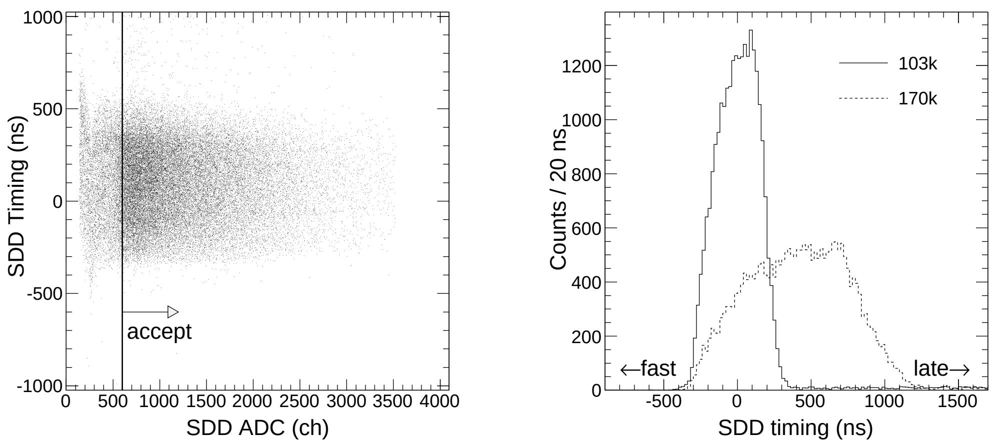

Figure 3.10: (a) Correlation of the signal height and the timing after the slewing correction and the event selection. (b) Typical TDC spectrum at different SDD temperatures.

Optimal Operational Temperature

Measured energy and time resolution dependence on the SDD temperatures are shown in Fig. 3.11. It shows the energy resolution got worse at temperatures lower than 130 K. Below 100 K, we sometimes could not obtain x-ray signals. Usually, semiconductor detectors are operated at a low temperature (< 150 K) to suppress the current noise caused by thermally excited carriers and the frequent *reset* caused by leakage current. However, the performance of an FET is known to become poor at such low temperatures. Our result may be explained by a such behavior of the FET on the SDD.

In the higher temperature region > 150 K, different tendencies were observed for different SDDs. However, this region is out of our interest for the operation and we can neglect the difference.

Considering that the time resolution becomes better at a lower temperature, 110 K - 130 K is the optimal operational temperature for the SDD. A further fine tuning will be done in the final setup.

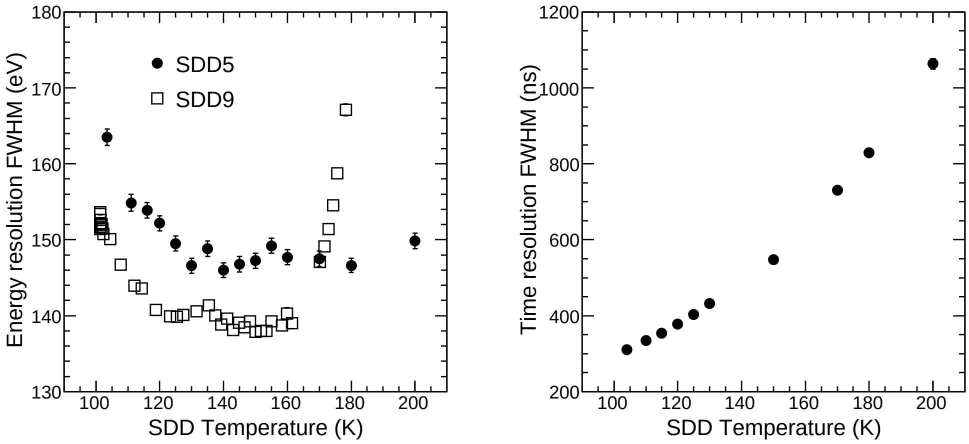

Figure 3.11: SDD temperature dependence of (a) the energy resolution at Mn K_α (b) the time resolution

Time Resolution and Electron Drift Time in Silicon

The observed temperature dependence of the time resolution can be well explained by the temperature dependence of electron mobility in silicon since the SDD time resolution reflects the electron drift time distribution in silicon. We calculated electron mobilities in SDDs from the measured time resolutions assuming the drift time from the outer-most ring to center anode corresponds to the resolution (FWHM), that is,

$$\mu_e = \frac{L^2}{FWHM \times (V_{RX} - V_{R1})} \tag{3.1}$$

where μ_e is an electron mobility, L is a length from the outer-most ring to the center anode, $FWHM$ is the measured time resolution, V_{RX} and V_{R1} are the applied voltages to the outer-most ring and inner-most ring, respectively. Figure 3.12 shows the estimated electron mobilities in SDDs are consistent with well-known data [25].

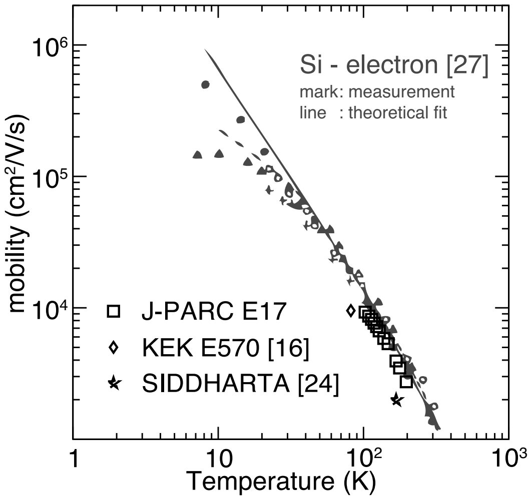

Figure 3.12: Electron mobilities in SDDs

Gain and Electron-Hole Creation Energy

We also found that Mn K_α peak position moves $\sim$0.5 eV equivalent every 1 K change, which is mainly due to the temperature dependence of the electron-hole pair creation energy [26].

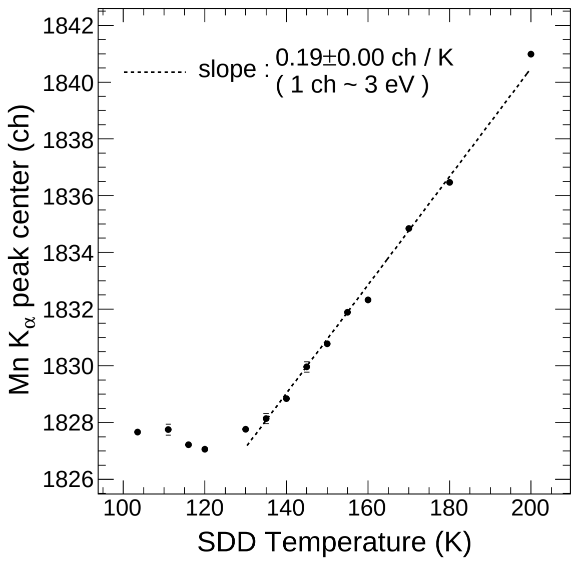

Figure 3.13: SDD temperature dependence of Mn K_α peak position

Chapter 4

Response Function of SDDs

As already mentioned in the introduction, most part of the systematic error in E570 came from the uncertainty of the response function of SDDs. The rest part of the systematic error in E570, which came from the validity of the energy scale, was also closely related to the response function. Therefore, studies of response function in various conditions are crucial for the suppression of the systematic error in E17.

4.1 Response Function

It is well known that the response of semiconductor detecter for monochromatic energy x-rays does not simply result in a symmetric Gaussian peak represented by the detector resolution. Following the E570 case, we use a response function based on that of conventional Si(Li) detectors intensely studied in many literatures [27].

We define the response function for characteristic x-rays as a summation of following 4 components.

$$
\begin{aligned}
Gauss(E) &= \frac{Gain}{\sqrt{2\pi}\sigma}\exp\left(-\frac{(E-E_0)^2}{2\sigma^2}\right) && (4.1)\\
Tail(E) &= \frac{F^G_{tail}\cdot Gain}{2\beta\sigma}\exp\left(\frac{E-E_0}{\beta\sigma}+\frac{1}{2\beta^2}\right)\\
&\quad\cdot\mathrm{erfc}\left(\frac{E-E_0}{\sqrt{2}\sigma}+\frac{1}{\sqrt{2}\beta}\right) && (4.2)
\end{aligned}
$$

$$Shelf(E) = \frac{F^{G}_{shelf-height} \cdot Gain}{2} \mathrm{erfc}\left(\frac{E-E_0}{\sqrt{2}\sigma}\right) \tag{4.3}$$

$$Esc(E) = \frac{F^{G}_{esc} \cdot Gain}{\sqrt{2\pi}\sigma} \exp\left(-\frac{(E-(E_0-E_{SiK_\alpha})^2}{2\sigma^2}\right) \tag{4.4}$$

$$\text{where,} \qquad \mathrm{erfc}(x) = \frac{2}{\sqrt{\pi}}\int_x^\infty e^{-t^2}dt \tag{4.5}$$

As a main peak, a Gaussian is used ($Gauss$) since the natural widths of characteristic x-rays are much smaller than the energy resolution of an SDD. Incomplete charge collections result in the structures in the low energy side, represented by $Tail$ and $Shelf$ in our case. $Tail$ is a convolution of an exponential, a step function and a Gaussian, while $Shelf$ is a convolution of a step function and a Gaussian. Escapes of a silicon K x-ray make a peak (Esc) which have indeed more complicated line shape than a simple Gaussian.

The definitions of the parameters appeared in above equations are described in Table 4.1. E_{SiK_α} is not a parameter but the energy of silicon K_α x-ray. Note that a *Pileup* component, which was appeared in E570, is not included in our response function since we succeeded to reject pileup events as will be described in Sec. 4.3. Figure 4.1 shows typical result of spectrum fitting with the response function defined here.

For some reason, we observed a peak just located at the Ti K_α energy. The peak seem to be actually Ti x-rays originated around the ^{55}Fe source since the peak disappeared when we attached a thick attenuator on the source. Therefore, we usually included Ti K x-rays represented by Gaussians in the fitting function for the ^{55}Fe spectrum.

Table 4.1: Definitions of the parameters in the response function.

structure	parameter	Description
	$Gain$	Area of Gaussian
$Gauss$	E_0	Mean value of the Gaussian
	σ	Width of the Gaussian. FWHM(=$2\sqrt{2\ln 2}$) was often used instead.
$Tail$	F^G_{tail}	Area ratio between the $Tail$ and the $Gauss$
	β	Slope of the $Tail$ structure
$Shelf$	$F^G_{shelf-height}$	Ratio between the $Shelf$ height and the $Gauss$ area
Esc	F^G_{esc}	Area ratio between the Esc and the $Gauss$

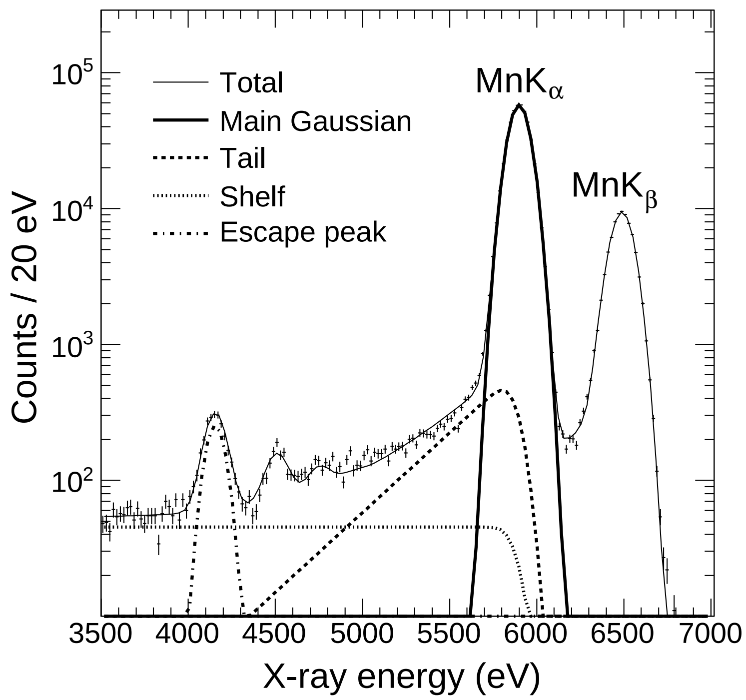

Figure 4.1: Typical ^{55}Fe spectrum fitted with the response function

To precisely evaluate these parameters in the response function is the purpose of the studies in the following sections.

4.2 Energy Dependent Energy Resolution

The energy resolution of a semiconductor detector is known to derive from noise and the statistical fluctuation in the number of created electron-hole pair. Therefore it can be given by

$$\Delta E(E) = 2.35\omega\sqrt{W_N^2 + \frac{FE}{\omega}} \tag{4.6}$$

where ω is the electron-hole creation energy in silicon, W_N and F denote a white noise and the Fano factor respectively.

The energy dependence of the energy resolution described by Eq. 4.6 will be used and confirmed later.

4.3 Pileup Rejection

To reject pileup events is important not only for the suppression of the systematic error in the fitting of the final spectrum, but also for the study of response function. Since pileup events disturb the spectrum, we cannot study detailed line shape without rejecting them.

4.3.1 Pre-pileup Event

To understand the pileup events, we first observed the signal baseline height just before an x-ray detection and checked the correlation with the signal height. The observation of the signal baseline was realized by a ~ 3 μs cable delay to be in time for the trigger. The timing relation of the trigger, signal and the delayed signal for the observation of the baseline is shown in Fig. 4.2 and Fig. 4.3. Since the baselines lay around the ground level, we set some offset in the CAEN shaping amplifier and used XOUT to enlarge the narrow distribution.

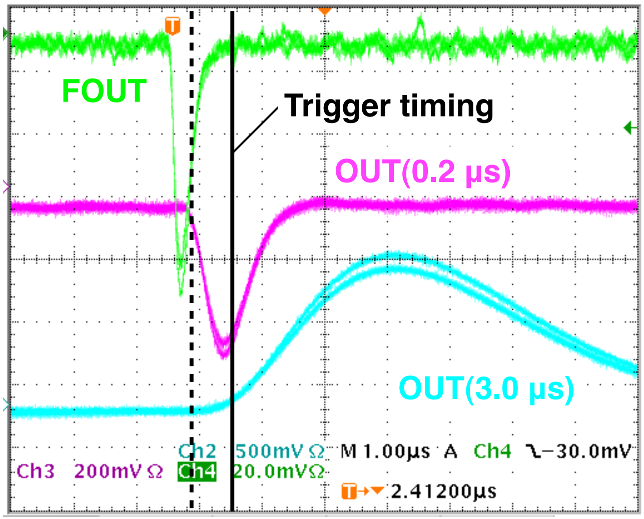

Figure 4.2: Timing relation of FOUT, OUT (shaping time = 0.2 μs) and OUT (shaping time = 3.0 μs)

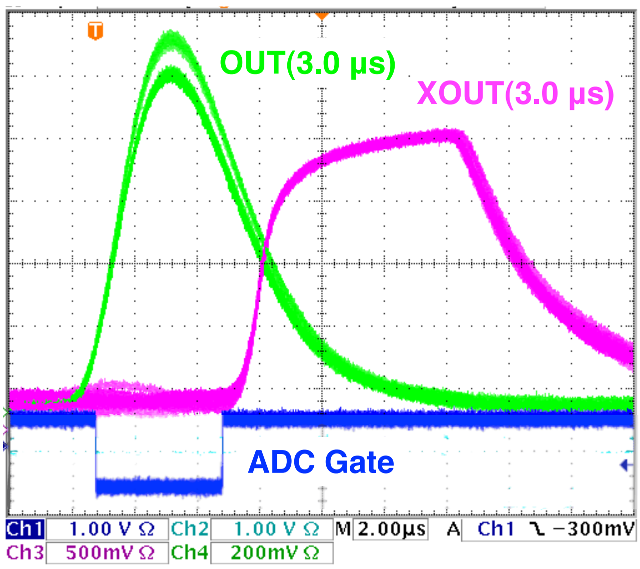

Figure 4.3: Timing relation of OUT, delayed XOUT and the ADC gate

^{55}Fe x-ray were observed in the background of ^{90}Sr electrons which realized a similar condition to an in-beam condition. The obtained correlation between the signal height and the baseline height is shown in Fig 4.4. Pileup events were clearly seen as tail structures toward higher baseline side and the x-ray spectrum became clean by removing those events with high baselines (Figure. 4.5). The data were obtained at the HighTh rate of $\sim$ 500 Hz.

However, the tail structure of the pileup events continues even beneath the gaussian peak in the baseline histogram. We estimated these events by fitting the baseline histograms with a Gaussian and a exponential tail structure ($Tail(x)$: a convolution of a Gaussian, an exponential and a step function). The line shapes were well represented by this fitting function as shown in Fig. 4.6. Then the ratios of the remained pileup events $F_{pile}^{3\sigma cut}$ were derived by a simple formula,

$$F_{pile}^{3\sigma cut} = \frac{\int_0^{G_{mean}+3\sigma} Tail(x)dx}{Gaussian \text{ area}} \tag{4.7}$$

The resulting ratio had linear dependence on the HighTh rate and it was $\sim$ 1% at the HighTh rate of several hundreds Hz, which is an expected rate in the realistic beam condition.

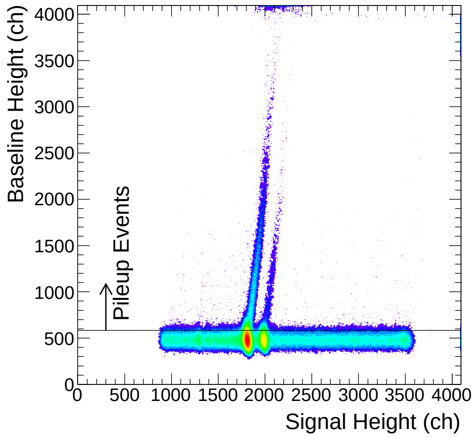

Figure 4.4: Correlation between the baseline and the signal height before the optimization of the veto widths.

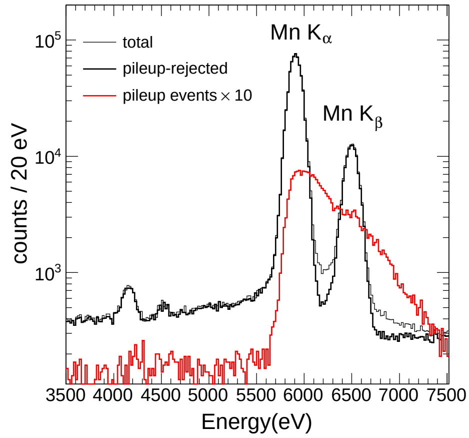

Figure 4.5: ^{55}Fe spectrum w/ and w/o the baseline cut (before the optimization of the veto widths).

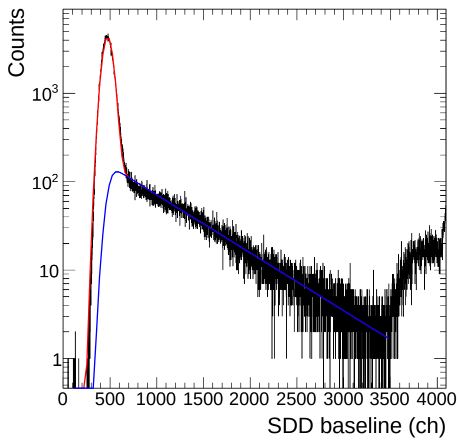

Figure 4.6: Base line histograms were fitted to estimated the ration of the remained pileup events after 3-sigma cut.

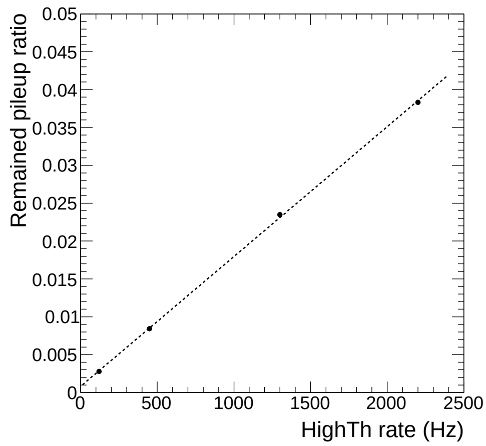

Figure 4.7: Ratios of the remained pileup events after the baseline 3-sigma cut.

Actually, most of these pre-pileup events occurred after vetoed signals induced by electron hits. Since a large signal sometimes takes more than 100 μs to recover the original baseline, the veto time for them should be set long enough. Then, we became almost free from pre-pileup events as shown in Fig. 4.8 and the baseline histograms are compared in Fig. /refbaseline. The HighTh rates were ∼500 Hz in both Figures.

In this method, there should be no remained pileup events unlike the case before the veto width optimization. It can be confirmed by analyzing Flash-ADC wave-form data obtained in the beam commissioning (Sec. 5).

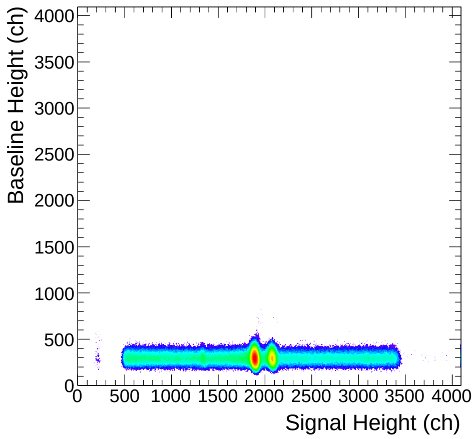

Figure 4.8: Correlation between the baseline and the signal height after the veto widths optimization.

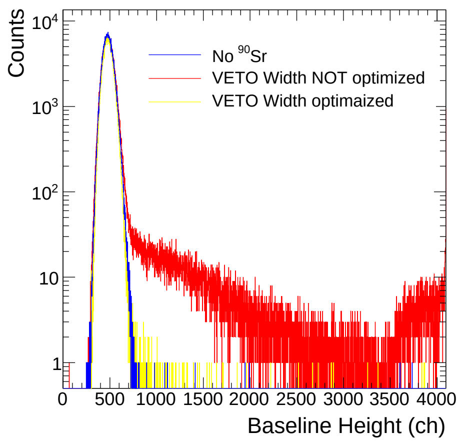

Figure 4.9: Histograms of the baselines in different conditions.

4.3.2 Post-pileup Event

A rejection of post-pileup events is much more complicated because they are much rarer than the pre-pileup events and the criteria of the pileup are not so clear. We recorded the charge of the signal tail and the timing of the next signal, then checked the correlation with the signal height. Although we could pick up some candidates of post-pileup events, we could not see whether or not they really disturbed the spectrum.

Again, Flash-ADC data should be useful to identify the post-pileup events.

4.4 Response at Different Detection Rates

4.4.1 X-ray Detection Rate

First, we checked the responses at different injection rates of x-rays by using two different intensity ^{55}Fe sources. Typical detection rates were ∼5 Hz and 3.2 kHz. Although the detection rate differed by 3 orders of magnitude and the relative intensities of Ti contamination and Mn K_β were different, we can not see differences in the spectral shape around Mn K_α peak (Fig. 4.10). The fitting results also showed no significant difference (Table. 4.2). The energy scale was determined by the Mn K_α and Mn K_β peaks and the conversion between an energy and an ADC channel was done via

$$\text{ADC channel} = \text{E2ch} \times \text{energy} + \text{Intercept}.$$

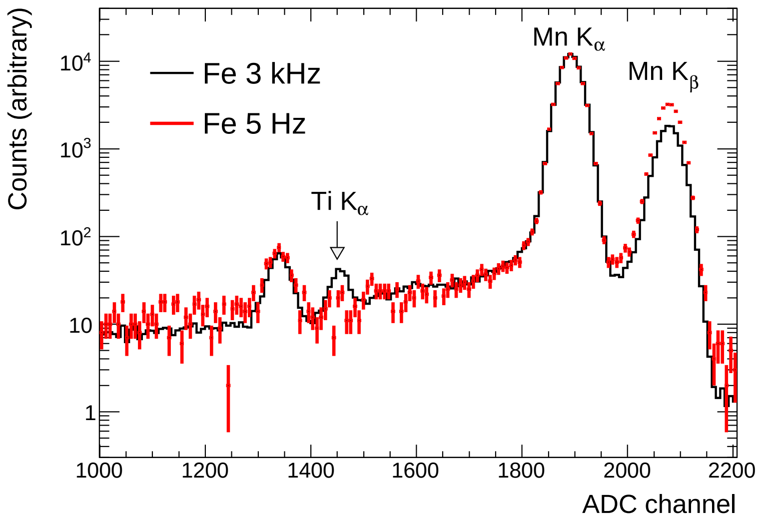

Figure 4.10: Comparison of the x-ray spectra at different incident x-ray rates normalized by the height of the Mn K_α peak.

Table 4.2: Comparison of the parameters in the response function at the different x-ray detection rates.

Parameter	High rate (3.2 kHz)		Low rate (5Hz)	
	value	error	value	error
E2ch	3.1462.E-01	9.3.E-05	3.1457E-01	6.3.E-06
Intercept	3.722.E+01	5.5.E-01	3.699E+01	3.8.E-02
Mn K_α Gain	7.906.E+06	8.3.E+03	5.647.E+05	2.2.E+03
Mn K_β Gain	1.250.E+06	3.5.E+03	1.639.E+05	1.3.E+03
Ti K_α Gain	1.828.E+04	5.3.E+02	9.9.E+01	9.2.E+01
Mn K_α FWHM (eV)	146.05	0.13	146.17	0.42
Mn K_β FWHM (eV)	155.54	0.21	155.94	0.66
Mn K_α Tail F^G_{tail}	2.31.E-02	3.9.E-04	2.05.E-02	1.5.E-03
Mn K_β Tail F^G_{tail}	1.06.E-01	1.8.E-03	8.25.E-02	4.1.E-03
Mn Tail β	4.54	0.10	4.25	0.36
Mn Shelf $F^G_{shelf-height}$	1.49.E-05	2.5.E-07	1.45.E-05	8.5.E-07
Mn Esc F^G_{esc}	4.05.E-03	8.1.E-05	4.67.E-03	3.1.E-04

4.4.2 Charged Particle Detection Rate

The responses at different detection rates of charged particles had investigated by changing electron hit rates from ^{90}Sr source while an ^{55}Fe source position was fixed during the measurement. The electron hit rate was defined by a scaler count of $HighTh$, which ranged up to 3 kHz. A typical x-ray detection rate was $\sim$ 50 Hz.

Because of the existence of the background induced by electrons as the typical spectra shown in Fig. 4.11, we could not correctly extract all the parameters of response function by the global fitting. To minimize the bias due to the background shape, local fits around the main peaks and the escape peak of Mn K_α were performed to extract the energy resolution, the $Tail\ F^G_{tail}$ and the $Esc\ F^G_{esc}$. $Tail\ \beta$ was fixed in the fitting. The obtained parameters are plotted against the detection rate of electrons in Fig. 4.12, which shows no systematic correlation.

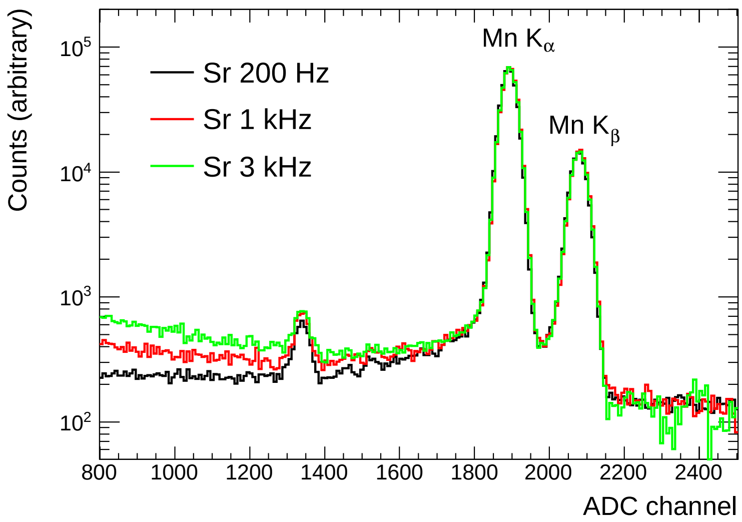

Figure 4.11: Comparison of the x-ray spectra at the different electron-background rates. Offsets were adjusted by the integral between 2200 and 2800 channel, and the spectra were normalized by the height of the Mn K_α peak.

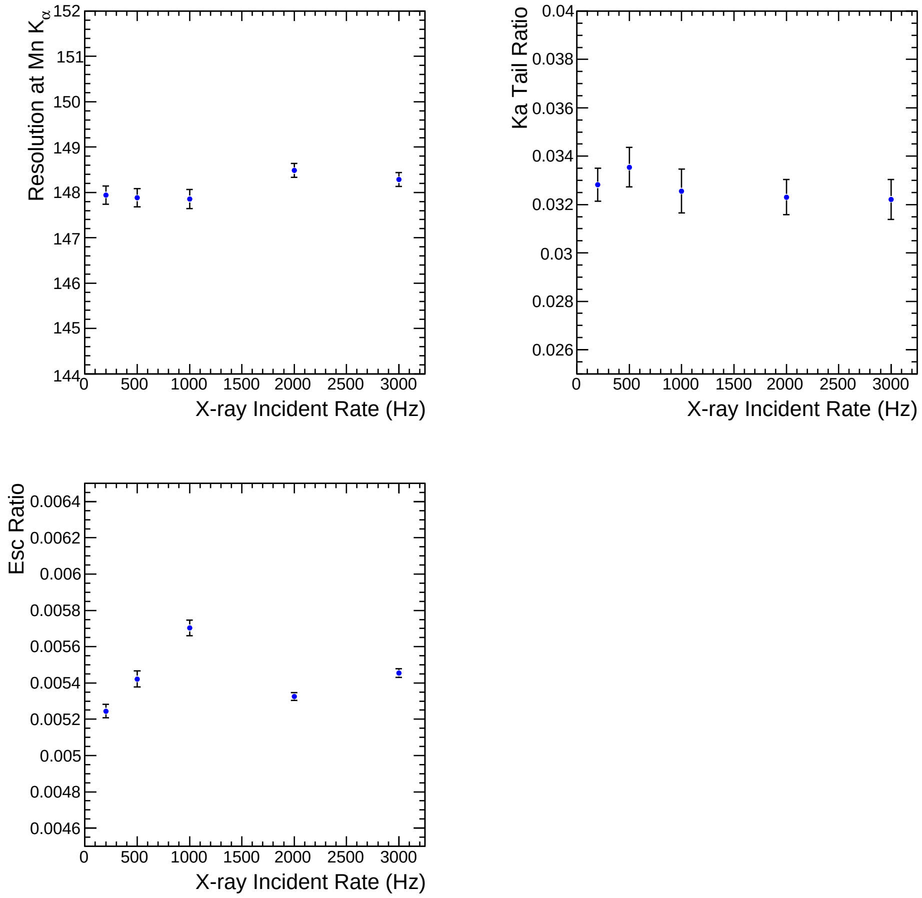

Figure 4.12: Dependence on the ^{90}Sr electron hit rate.

As we employ the in-situ calibration method, the rate dependence of the response function make little trouble for us even if it existed. But these measurements guarantee that the parameters obtained in the source measurements can be applied for the spectrum under the beam condition.

4.5 Response to Different Incident Angles

Because of the low statistics of kaonic helium x-rays, the parameters of their response function cannot be determined by themselves. One possible method to estimate them is an interpolation from the parameters of the calibration lines. However, the incident-angle distributions of the calibration x-rays and kaonic helium x-rays are completely different in E17 as shown in Fig. 4.13. In this context, the response of SDDs to different incident angles are of great interest.

The measurement was performed for the incident angle from 0 to 80 degrees. 80 degrees is almost the acceptance limit of SDDs in the housing. To cover this wide range of incident angle, the SDD housing was tilted by 45 degrees in the test cryostat and the incident angle was changed by the ^{55}Fe source position (Figure 4.14).

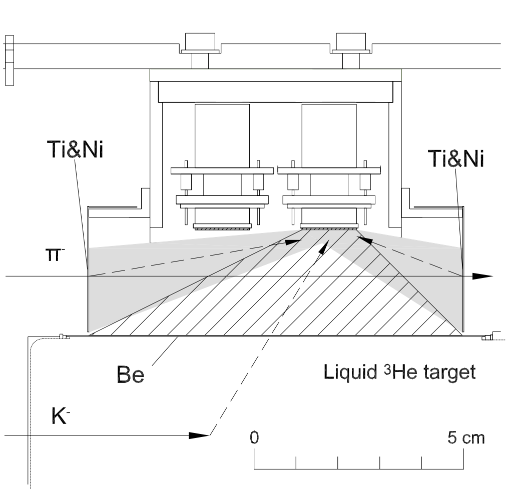

Figure 4.13: Close up view around the E17 target.

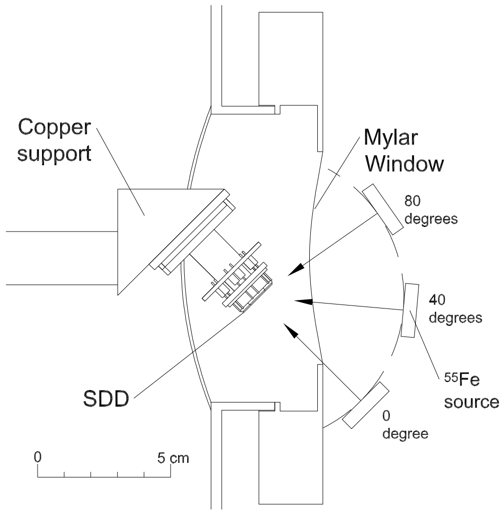

Figure 4.14: Schematic of the setup for angle measurements.

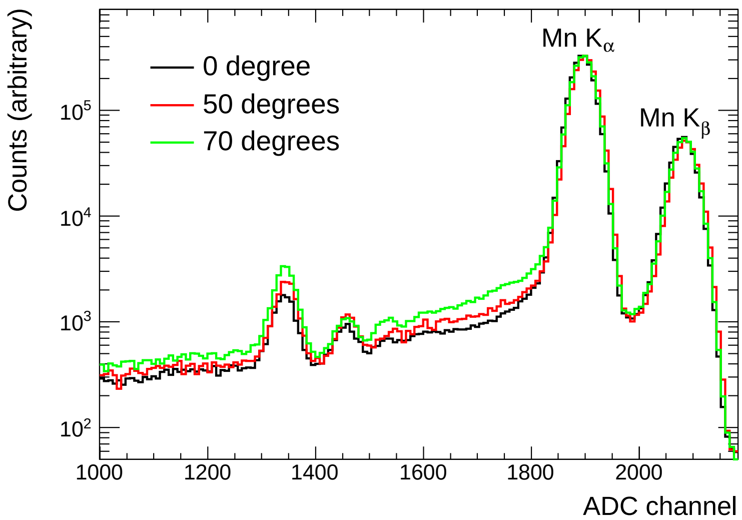

Figure 4.15: Comparison of the x-ray spectra to the different incident angle normalized by the height of the Mn K_{α} peak.

The typical spectra are shown in Fig. 4.15 and the fitting results with the response function are plotted in Fig. 4.16. Although the resolutions were stable for wide range of incident angle, significant dependences on incident angle were observed for $Tail\ F^{G}_{tail}$, $Shelf\ F^{G}_{shelf-height}$, $Esc\ F^{G}_{esc}$.

A possible explanation of these tendencies is as follows. Almost all Incident x-rays (several keV in our case) are absorbed by the photoelectric effect in silicon. The generated low-energy photoelectrons distribute mainly in the perpendicular direction to the incident x-rays. In addition, the effective surface become thicker as the incident-angle become larger. Thus, with a larger incident angle, both electric charges and silicon x-rays are easy to escape from the sensitive region, resulting in higher intensities in the components in the lower energy side of the main peak.

The effect of different incident angle to the peak center position (mean value E_0 of Gaussian) will be discussed in the next section.

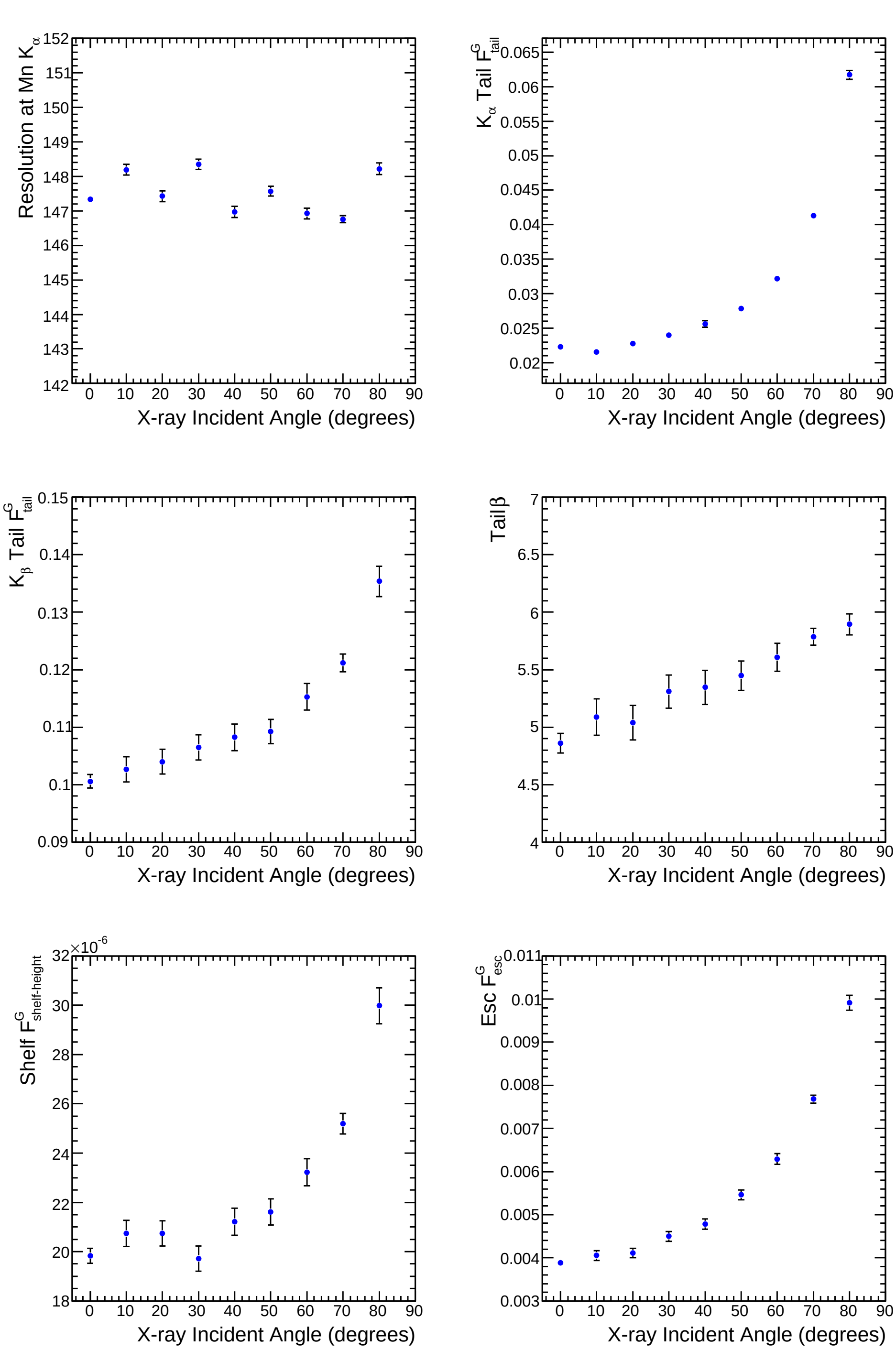

Figure 4.16: Dependence on the incident angle.

4.6 Validity of the Calibration Method

"The Calibration Method" includes following elements here.

- Absolute energy calibration by using the characteristic x-rays of titanium and nickel.
- Response function as a fitting function for the x-ray spectrum
- Different incident-angle effect
- Linearity of the whole system

For the study of these things, we obtained the fluorescence x-ray lines of titanium and nickel induced by ^{90}Sr electrons in addition to the manganese lines from ^{55}Fe.

For the two spectra with different incident-angle manganese x-rays (0 and 60 degrees), various spectral fittings were performed to evaluate the energy of Mn $K_{\alpha 1}$ peak center ($E^{meas.}_{MnK_{\alpha 1}}$) from the interpolated value from the Ti $K_{\alpha 1}$ and Ni $K_{\alpha 1}$ peak positions and their known energies (Table. 3.4). Then, the Mn $K_{\alpha 1}$ energy deviation was defined by

$$\Delta E_{MnK_{\alpha 1}} = E^{meas.}_{MnK_{\alpha 1}} - E^{ref}_{MnK_{\alpha 1}}$$

where $E^{ref}_{MnK_{\alpha 1}}$ is the reference energy in Table 3.4.

Fitting Function and Parameters

As for a fitting function, the response function defined in Sec.4.1 was used for $K_{\alpha 1}$, $K_{\alpha 2}$ and K_{β} lines of titanium, manganese and nickel. The background was estimated to be a second order polynomial function. Because the background shape become nontrivial in the low channel, the fitting ranges were limited and thus Esc peaks for the titanium lines were omitted.

Best Fit

Figure 4.17 shows the fitting spectra which seem to give the most reliable fitting parameters. They relatively well reproduced the parameters obtained in Sec. 4.3. Therefore, we set this fitting condition as a standard, and examined what happens if the fitting condition changed a bit.

Note that χ^2/ndf became bad with higher statistics spectrum (even in an ^{55}Fe spectrum with almost no backgound). It might be because the weak components such as the RAE (radiative auger electron) peaks, the satellite peaks and contaminating x-ray lines revealed their significance. Furthermore, the response of the SDD is indeed much complicated than our relatively simple description. However, our goal is to know the energy of the peak centers which will be clearly observed. Therefore we do not necessarily fit the whole spectrum well, although the statistical effects from the bad fitting should be carefully considered.

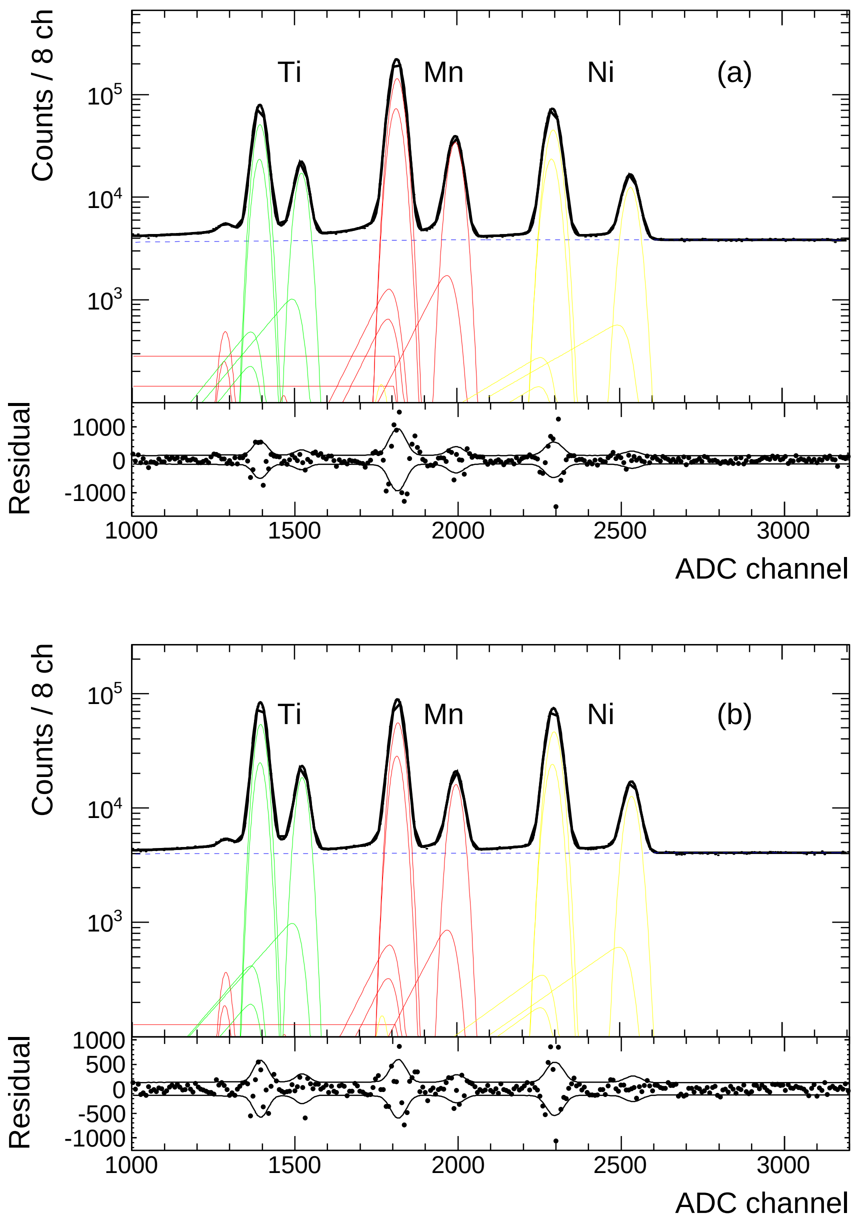

Figure 4.17: Obtained spectra for the study of the validity of the calibration method. (a) ^{55}Fe: 0 degree, (b) ^{55}Fe 60 degree. Residuals of the fittings are also shown with $\pm 2\ \sigma$ lines.

Table 4.3: Obtained parameters by the "Best Fit". Ni *Esc* F^G_{esc} was fixed since the Ni *Esc* peaks overwrap with Mn K_α peak.

Parameter	0 degree		60 degrees	
	value	error	value	error
E2ch	3.03862.E-01	2.4.E-06	3.0423.E-01	1.8.E-05
Intercept	2.330.E+01	1.9.E-02	2.360.E+01	1.1.E-01
Mn K_αGain	1.053.E+07	1.1.E+04	4.068.E+06	7.5.E+03
Mn K_βGain	1.724.E+06	4.9.E+03	8.023.E+05	5.3.E+03
Ti K_αGain	3.314.E+06	5.4.E+03	3.484.E+06	6.7.E+03
Ti K_βGain	7.894.E+05	2.7.E+03	8.395.E+05	4.1.E+03
Ni K_αGain	3.666.E+06	5.8.E+03	3.716.E+06	6.3.E+03
Ni K_βGain	6.895.E+05	2.9.E+03	6.929.E+05	3.7.E+03
Mn K_α1Shift	-1.79.E-01	1.1.E-01	-3.54.E-01	1.7.E-01
Mn K_β1Shift	-3.01.E+00	2.1.E-01	-3.89.E+00	4.4.E-01
Ti K_β1Shift	-1.41.E+00	2.9.E-01	-1.28.E+00	3.4.E-01
Ni K_β1Shift	-3.81.E+00	3.7.E-01	-3.94.E+00	4.5.E-01
Mn K_αFWHM	150.22	0.12	149.17	0.23
Ti K_αFWHM	137.54	0.21	136.56	0.23
Ni K_αFWHM	164.09	0.20	162.69	0.23
Mn K_α F^G_{tail}	2.04.E-02	6.8.E-04	2.84.E-02	2.9.E-03
Mn K_β F^G_{tail}	1.16.E-01	3.3.E-03	1.33.E-01	9.3.E-03
Ti K_α F^G_{tail}	3.31.E-02	1.3.E-03	3.05.E-02	2.4.E-03
Ti K_β F^G_{tail}	2.04.E-01	6.2.E-03	2.10.E-01	2.1.E-02
Ni K_α F^G_{tail}	3.21.E-02	1.6.E-03	3.71.E-02	2.7.E-03
Ni K_β F^G_{tail}	2.42.E-01	1.6.E-02	2.40.E-01	2.5.E-02
Mn Tail β	3.49	0.16	3.95	0.62
Ti Tail β	6.30	0.20	7.46	0.86
Ni Tail β	10.85	1.22	10.02	1.36
Mn Shelf $F^G_{shelf-height}$	2.98.E-05	6.4.E-05	2.82.E-05	6.3.E-05
Ti Shelf $F^G_{shelf-height}$	1.00.E-09	3.1.E-06	1.01.E-09	6.5.E-06
Ni Shelf $F^G_{shelf-height}$	4.06.E-05	8.7.E-07	4.75.E-05	1.7.E-05
Mn Esc F^G_{esc}	3.07.E-03	1.6.E-04	5.87.E-03	5.2.E-04
Ni Esc F^G_{esc}	3.00.E-03	fixed	3.00.E-03	fixed
BG p0	3.288.E+03	6.1.E+00	3.90.E+03	2.3.E+02
BG p1	4.53.E-01	1.8.E-03	7.43.E-02	1.7.E-01
BG p2	-8.93.E-05	9.1.E-07	-8.35.E-06	3.2.E-05
χ^2	752.4		562.4	
NDF	244		244	

Asymmetric Gaussian

Characteristic x-ray lines are known to have asymmetric shape due to the existence of satellite lines which resulted from the possible existence of additional holes in the outer shell. The additional holes can be created by the charged particle hits, thus asymmetric shapes appear for the titanium and nickel lines and not for manganese line.

The asymmetric Gaussian peak made the peak energy $\sim$ 0.3 eV lower compared to the symmetric Gaussian case, which is consistent with the Monte Carlo study described in Appendix A. Although the energy deviation became larger for the present spectra, the asymmetric one was adopted in the following fittings.

Table 4.4: Energy deviations for symmetric and asymmetric *Gauss*. χ^2/ndf is represented by the values of 60 degrees (same in the following tables).

Gaussian	$\Delta E_{MnK_{\alpha 1}}$ (eV) 0 degree	60 degrees	χ^2/ndf
Asymmetric	-0.18	-0.35	562.4/244
Symmetric	0.16	-0.02	561.9/244

Treatment of Tail Slope

The energy deviation became significantly larger with common *Tail* slope β for all 6 peaks. As the "best fit" implies β depends on the energy, we should check it.

Individual βs for all 6 peaks gave some unrealistic β values although the energy deviation and the reduced chi-square became better.

Table 4.5: Difference in the energy deviations by the treatment of the $Tail$ slope β.

$Tail\ \beta$	Tail β	$\Delta E_{MnK_{\alpha 1}}$ (eV)		
Ti/Mn/Ni	K_α/K_β	0 degree	60 degrees	χ^2/ndf
individual	common	-0.18	-0.35	562.4/244
common	common	-0.59	-0.76	580.7/245
individual	individual	+0.07	-0.20	554.0/241

Shelf component

It is hard to correctly separate the weak $Shelf$ components from the background. However a treatment of them changed the peak position up to 0.2 eV.

Table 4.6: Difference in the energy deviations by the treatment of the $Shelf$ intensity ($F^G_{shelf-height}$) . fixed values were 2.0×10^{-5} / 2.5×10^{-5} for 0 degree / 60 degrees.

	$\Delta E_{MnK_{\alpha 1}}$ (eV)		
Shelf $F^G_{shelf-height}$	0 degree	60 degrees	χ^2/ndf
free	-0.18	-0.35	562.4/244
0	-0.42	-0.54	566.5/247
fixed	-0.34	-0.50	567.1/247

Background Shape

We changed the background shape to a linear one and a constant one. The difference of the obtained energy deviation was small ($<$ 0.1 eV).

Table 4.7: Difference in the energy deviation by the background shape.

	$\Delta E_{MnK_{\alpha1}}$ (eV)		
Background	0 degree	60 degrees	χ^2/ndf
pol2	-0.18	-0.35	562.4/244
linear	-0.28	-0.37	562.5/245
constant	-0.27	-0.40	563.2/246

Fitting Range

The changes in the upper limit only strengthen the constraint on the background parameters and did not affect the energy deviations. However, the changes in the lower limit had non-negligible effect to the energy deviation since the lower limits lay in the structure of titanium peaks.

Table 4.8: Difference in the energy deviation by the fitting range.

		$\Delta E_{MnK_{\alpha1}}$ (eV)		
lower limit	upper limit	0 degree	60 degrees	χ^2/ndf
1000	3200	-0.18	-0.35	562.4/244
1000	2800	-0.20	-0.32	477.0/194
1000	3000	-0.21	-0.35	534.7/219
1000	3400	-0.17	-0.36	597.3/269
900	3200	-0.28	-0.49	605.6/256
1200	3200	-0.33	-0.45	526.6/219

Effect of Incident Angle and Linearity of the System

The difference in $\Delta E_{MnK_{\alpha1}}$ between two incident angles was -0.17 ± 0.2 (stat.) eV in the best fit condition. Other fittings also coincided with this value within the statistical error. Note that the effect of the incident angle for the peak position can be evaluated almost independently from the other effects.

However, since the $\Delta E_{MnK_{\alpha1}}$ appears as a mixed effect of all the factor mentioned in the beginning of this section, it's difficult to discuss the linearity of the system alone. What we can say from this study is over all systematic uncertainty of the energy scale at 6 keV can be controlled conservatively below 1 eV in our system.

Further studies to check the validity of the energy scale should be done in the final setup.

Energy dependent resolution

From the obtained resolutions of three K_α lines, we checked the energy dependence of the energy resolution described by eq. (4.6) . ω is fixed to 3.81 eV, which is the known experimental value at 77 K although the SDD temperature was at ∼130 K in our measurements. The difference of ω value due to the temperature was absorbed to the Fano factor and the white noise.

Three resolutions were well fitted with eq. 4.6 and the obtained parameters are written in Table 4.9. The parameters of two different incident-angle coincided well and the obtained Fano factors were consistent to other experimental values (F ∼0.12)

Table 4.9: Obtained white noises and Fano factors.

spectrum	White Noise	Fano Factor
^{55}Fe 0 degree	9.15 ± 0.13	0.1280 ± 0.0016
^{55}Fe 60 degree	9.18 ± 0.13	0.1251 ± 0.0016

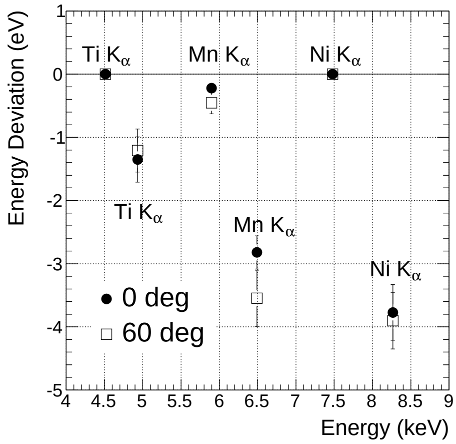

Figure 4.18: Energy deviations of the x-ray peaks.

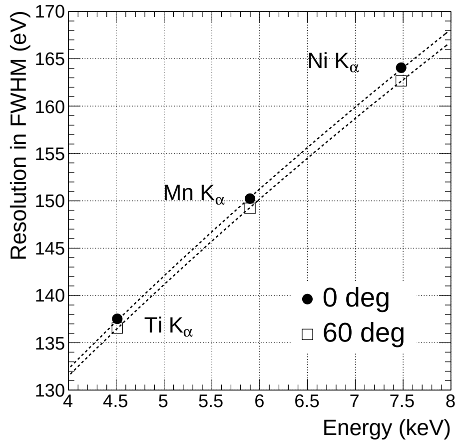

Figure 4.19: Energy dependent energy resolution.

Chapter 5

SDD Commissioning with the Beam

From November 8th midnight to November 11th morning in 2011, we used about 30-hour beam time for an SDD commissioning at the K1.8BR beamline in the J-PARC hadron experimental facility. The purpose of the beam commissioning was

- To confirm the SDD operation in the real beam condition.
- To investigate yields of characteristic x-rays and signal-to-noise ratio in the different beam intensity.

We observed characteristic x-rays from titanium, iron and nickel foils induced by the beam.

5.1 J-PARC

5.1.1 J-PARC

J-PARC consists of three proton accelerators, Linac as an injector, 3 GeV Rapid Cyclotron (RC), and 50 GeV Main Ring (MR). The concept of the accelerator complex is to utilize secondary particle produced by intense primary proton beam of 1 MW class. RC acts as a booster for MR while providing the beam to the Material and Life science Facility (MLF) where secondary muons and neutrons are used. MR, now operating at 30 GeV, provides a fast extraction (FX) beam to produce neutrino beam to Kamioka or a slow extraction (SX) beam to the hadron experimental facility, where mainly secondary kaons are used for the experiments.

Unfortunately, the accelerators still being in the commissioning stage, available beam intensity is limited especially for the SX beam.

5.1.2 K1.8BR Beamline in the Hadron Experimental Facility

The K1.8BR beam line, where our experiment is going to be performed, is located at the north side of the hadron experimental hall. As the name implies, we need to share beam with K1.8 beam line. The configuration of K1.8BR beam line is shown in Fig. 5.1 and its parameters are summarized in Table. 5.1.

K1.8BR has a rather long length of 31 m from the production target (T1) to the final focus point (FF), where the experimental target will be set. However, a 6-m-long Electrostatic Separator (ESS1), together with Correction Magnets (CM) and vertical slits (IF-V, MS1), has excellent particle separation power.

Since this beamline is a brand-new one, we are putting many efforts on beamline tuning. Especially for a stopped -K^- experiment, the tuning should be performed carefully, otherwise few kaons stop in the target.

Hardware online triggers for the particles (k, e, π, p) had been established and beamline study is well under way on the optics, acceptance of beamline ESS1 and slits, particle yields against momentum, central momentum of the beamline and so on. Now we are almost ready to stop kaons for the E17 physics run. A typical in-flight negative kaon yield at 0.9 GeV/c, which will be adopted momentum for E17, is 8 k/ spill with a primary proton beam intensity of 1 kW (1.2×10^{12} protons per pulse with a repetition cycle of 6 seconds) using the Pt production target. The stopped kaon number is expected to be more than two order of magnitude smaller.

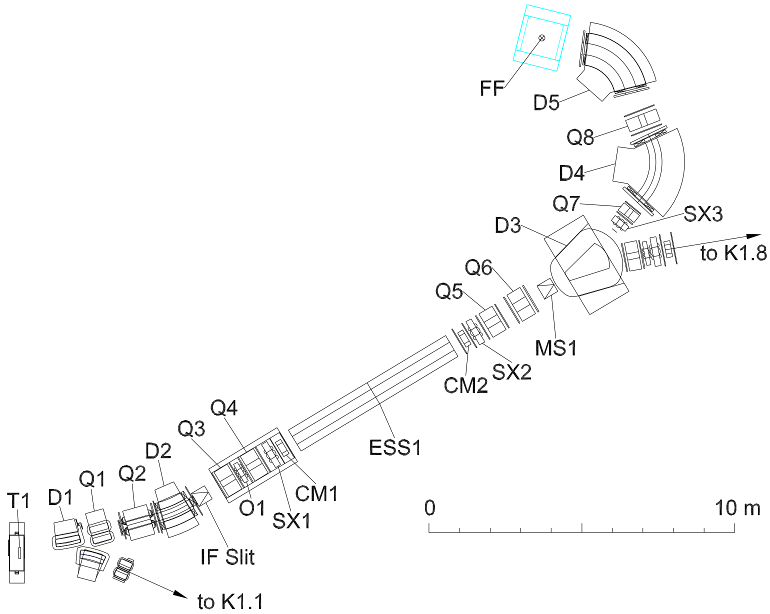

Figure 5.1: Schematic drawing of K1.8BR beam line in the J-PARC hadron experimental facility.

Table 5.1: Parameters of K1.8BR beam line as of November, 2010.

Primary beam	30 GeV/c proton
Repetition cycle	6 sec
Flat Top	2.93 sec
Spill Length	2.1 sec
Production target	Pt(50% loss)/Ni(30% loss)
Beam Length (T1-FF)	31.1 m
Momentum range	1.1 GeV/c max.
Acceptance	2.6 msr · %
Momentum bite	± 3 %

5.2 Setup

5.2.1 Beamline Detectors

At the down stream of the D5 magnet, a beam was detected by the T0 counter and Defining counter (Define) together with tracking information provided by the beamline drift chambers (BLC1 and BLC2). Although Lucite Cherenkov counters (LC2) are set for an online particle identification, they were not used for the present commissioning.

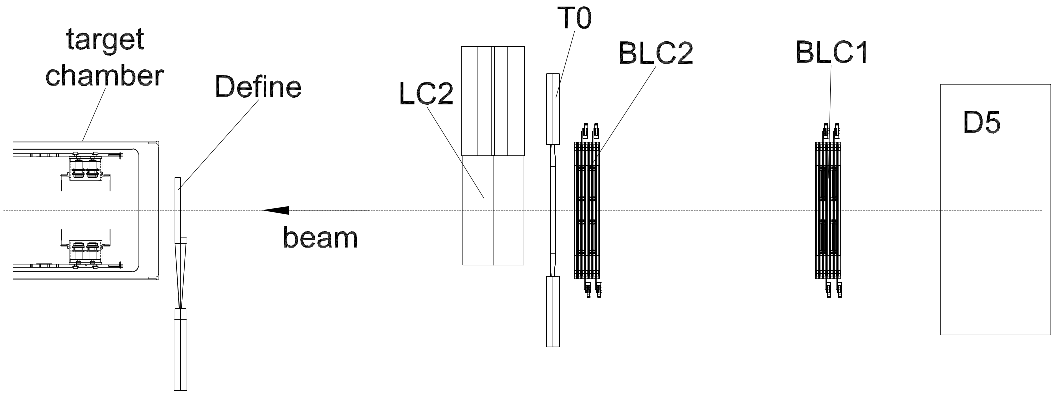

Figure 5.2: Side view of the detector alignment downstream the D5 magnet.

T0 counter

The T0 counter consists of 5 segmented scintillator hodoscopes. Each segment has 16 cm (vertical) $\times$ 3.2 cm (horizontal) effective area with a thickness of 1 cm. Two PMTs, HAMAMATSU 6612B, with three-stage boosters are mounted on the both ends of the each scintillator. The T0 counter was used to determine the timings of beam triggers.

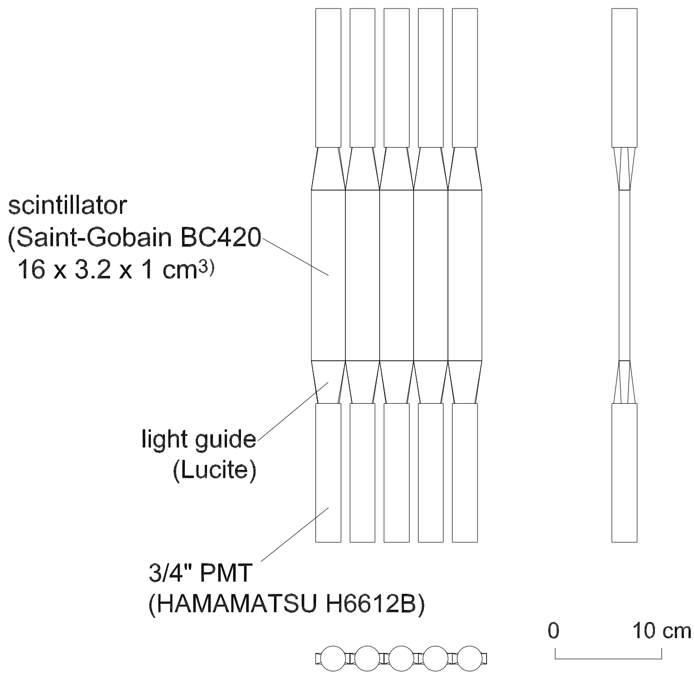

Figure 5.3: T0 counter.

Defining Counter

To suppress the trigger rate, we prepared an additional beam defining counter just in front of the target chamber. The plastic scintillator (BC420) is 1 cm thick and has the size of 12 cm (vertical) $\times$ 12 cm (horizontal), which just covered the foil positions inside the target chamber. One PMT, HAMAMATSU 6612B with three-stage boosters is attached on it.

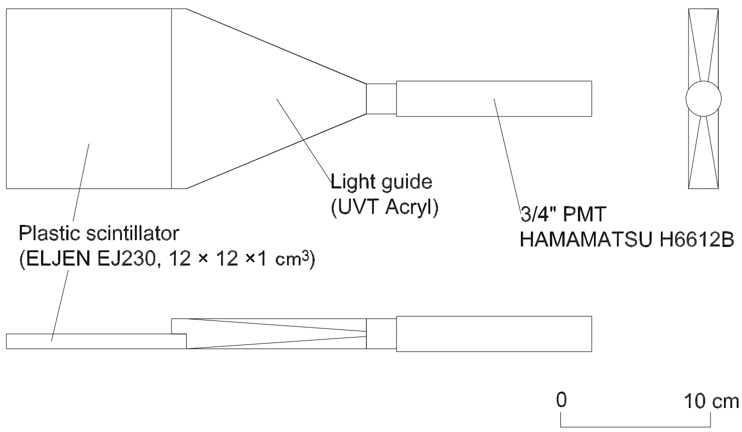

Figure 5.4: Defining Counter.

Beam Line Drift Chamber

BLC1 and BLC2 are planner drift chambers consisted of 8 layers (xx'yy'xx'yy'). The detailed description of BLCs is omitted here since their information is not used for the present analysis.

5.2.2 SDD & Liquid-^{3}He Target System

8 SDDs and corresponding 8 preamplifiers were installed to the target chamber as illustrated in Fig. 5.5. They were cooled by liquid nitrogen and temperatures were controlled with the similar method described in Chapter 3.

The liquid-^{3}He target was not installed and an iron foil was set instead, in addition to titanium and nickel foils which were located the same position as in the physics run.

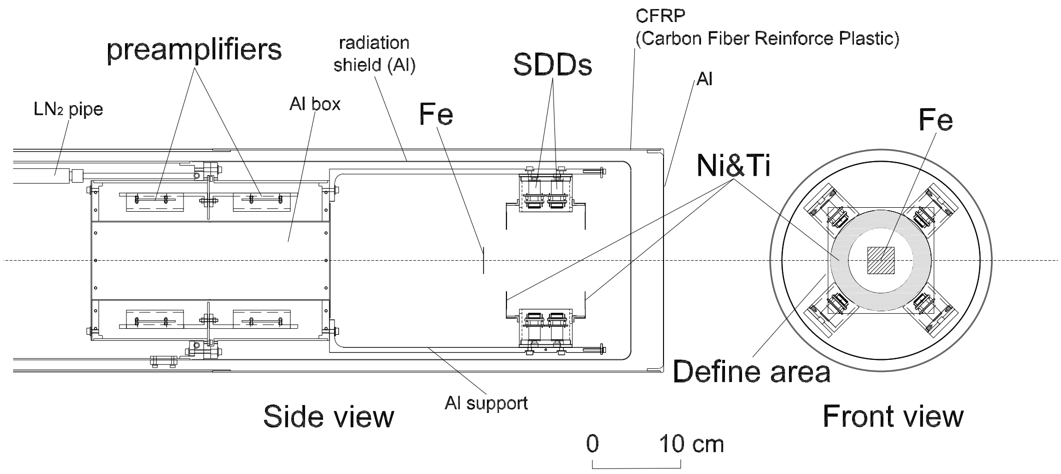

Figure 5.5: Front and side views of the SDD & liquid-^{3}He target system.

5.2.3 Trigger Scheme & Data Acquisition

An SDD trigger was defined as (Fig. 3.4 (c))

$$SDD = LowTh \otimes \overline{Reset} \otimes \overline{HighTh}$$

and a $BEAM$ trigger as

$$BEAM = Define \otimes T0_{retiming}$$

whose timing was determined by the T0 counter.

Then the master trigger was defined as

$$SDDOR \otimes BEAM + SDDself(SDDOR)$$

As is the case of the measurement in the test cryostat, we constructed TKO based data acquisition system including two major upgrades. One was the introduction of a second level trigger scheme and the other one was an additional DAQ system to use VME modules.

Second Level Trigger Scheme

Since SDD responses are very slow (1 μs), they are not in time to make gates for the signals of the fast detecters in the beam line (scintillation counters, drift chambers). Therefore, we need to make gates for the beam line detectors by $BEAM$ triggers. Then, if $SDDOR$ comes (doesn't come) within a certain time, the event is accepted (rejected) by using the VME-SMP functionality. The second level trigger circuit is shown in Fig. 5.6 and the settings for the gate and delay generators are listed in Table 5.2. Typical dead times of DAQ system for an accepted event and a rejected event were 690 μs and 5 μs, respectively.

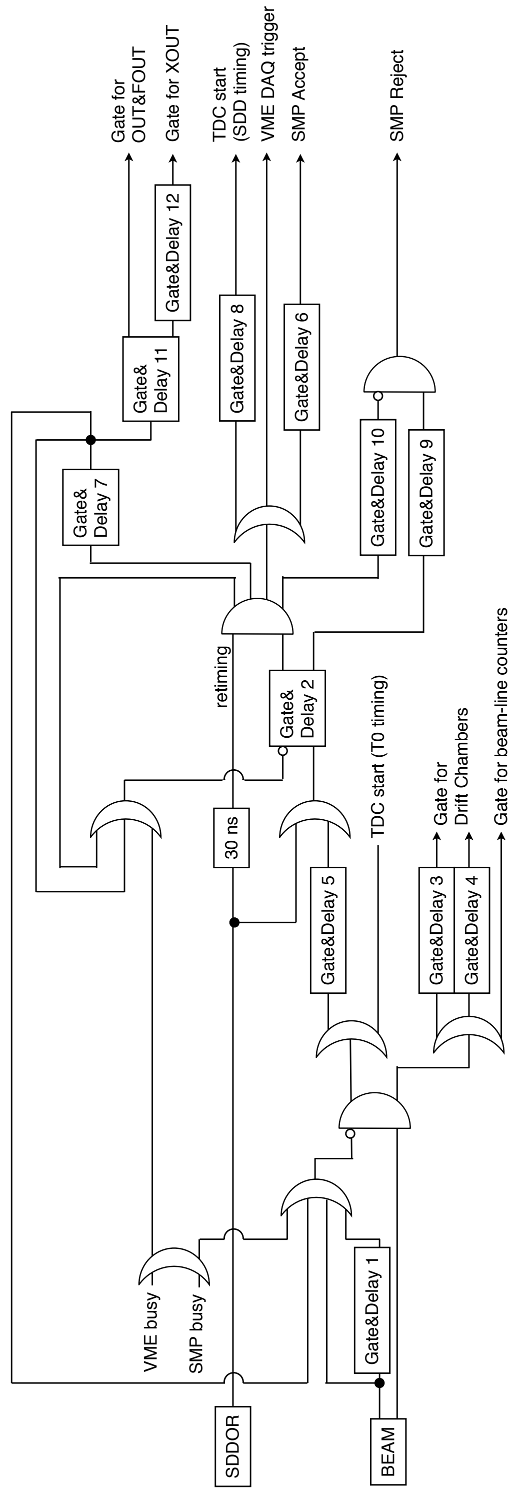

Figure 5.6: Second level trigger circuit

Table 5.2: Settings for the gate and delay generators in the second level trigger circuit.

Number	Delay	Width	Description
1	Through	3.3 μs	wait for second level decision
2	Through	2.0 μs	timing gate for second level decision
3	440 ns	1.52 μs	gete for beam line chambers
4	220 ns	1.45 μs	gate for beam line chambers
5	510 ns	30 ns	delay
6	390μs	80 ns	wait for conversion
7	Through	430 μs	conversion veto
8	Through	130 ns	TDC start
9	2.18 μs	40 ns	reject
10	Through	2.2 μs	reject veto
11	Through	5.3 μs	ADC gate for SDD OUT&FOUT
12	Through	2.1 μs	ADC gate for SDD XOUT
13	1.2 μs	390 ns	delay

Table 5.3: Thresholds of the discriminators and veto widths for the SDD trigger circuit.

	Discriminator V_{th} (mV)		Veto Width (μs)	
SDD #	LowTh	HighTh	Reset	HighTh
1	150.5	810	600	200
2	150.4	807	500	220
3	148.8	806	480	210
4	149.7	796	400	200
5	150.2	802	400	420
6	151.0	805	500	200
7	149.8	805	500	220
8	149.4	797	800	200

VME DAQ System

A VME DAQ system was prepared for a Flash ADC module and a Peak Hold ADC module which has a better linearity than the TKO PHADC module. These data were recorded in a separated file from the TKO data. Both TKO and VME data contained a spill number and an event ID distributed by a Master Trigger Module, which made it possible to synchronize two data offline.

The whole scheme of the data acquisition system is shown in Fig 5.7.

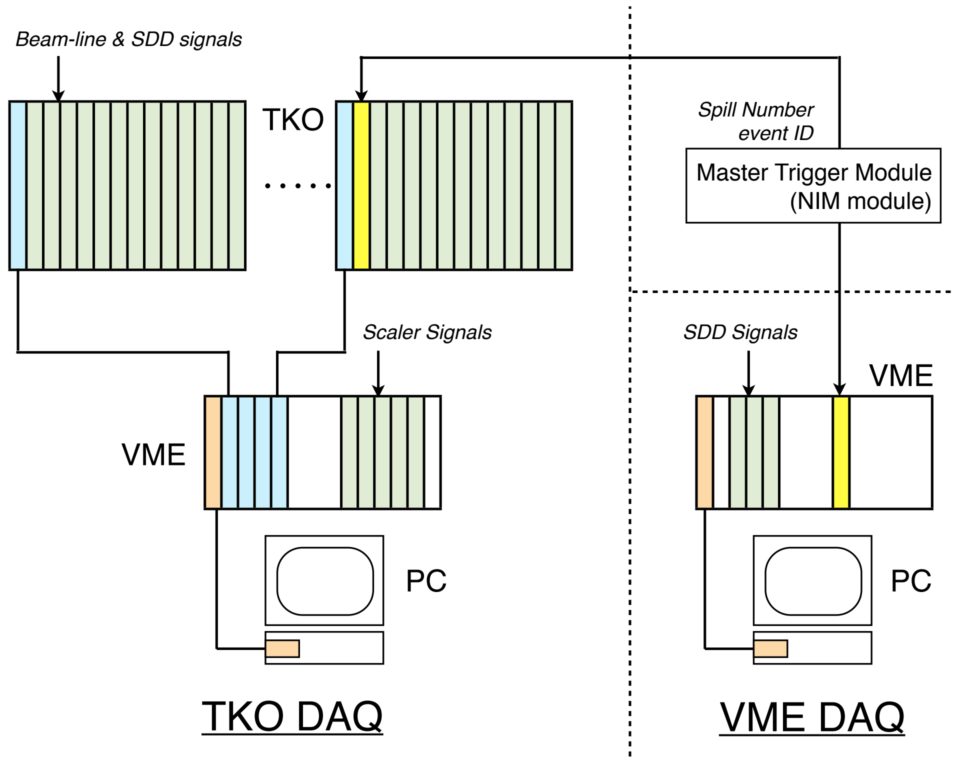

Figure 5.7: DAQ scheme in the SDD beam commissioning.

5.2.4 Experimental Condition

SDD Temperatures

All 8 SDDs showed similar behavior during the 3 days (Figure 5.8 (a)). They were kept at 132 $\sim$ 137 K with stabilities below 2 K. The gain difference due to these temperature changes were expected to be $\sim$ 1 eV (Sec. 3.4), which were compensated by the in-situ calibration anyway.

Preamplifier Temperatures

As for preamplifiers, some of them showed strange behavior (Figure 5.8 (b)). Temperatures of preamplifier #2 and #3 dropped when accelerator accidentally stopped. These phenomena implied that the ramped output from the preamplifier disappeared due to the low detection rate. We don't know, however, why these phenomena happened only to specific modules. Anyway, we observed no effect to the resolutions and the gain stabilities. The temperature sensor for preamplifier #7 was not available due to a problem in the read-out line.

However the temperatures of 7 preamplifiers ranged as large as 30 K, all of them were in the optimal region. The stabilities of each preamplifier temperature were satisfactory ($\sim$ 1 K).

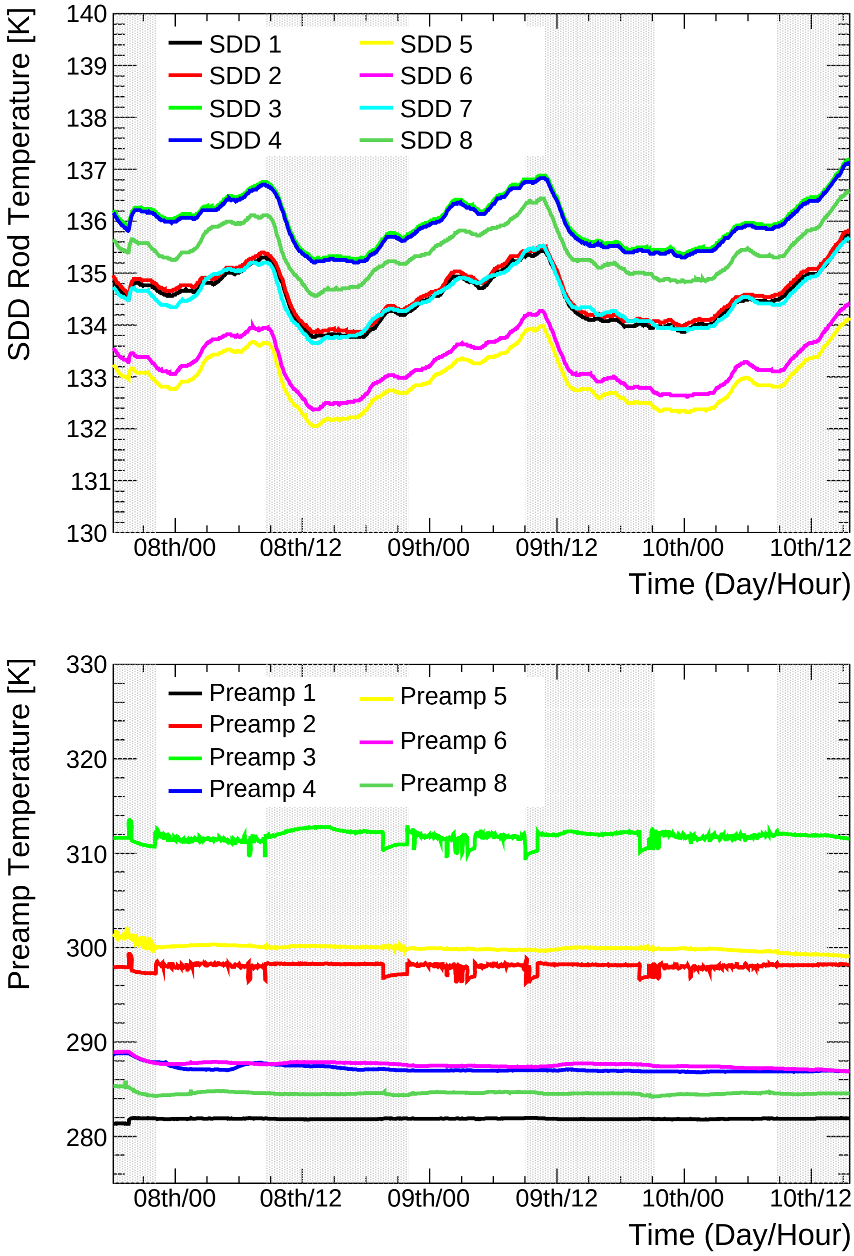

Figure 5.8: (a) SDD temperatures and (b) preamplifier temperatures during the beam time. Hatched areas indicate that the beam was off in those periods, when We put ^{90}Sr source instead.

5.3 Data Summary

We used -0.9 GeV/c kaon-tuned beam (ESS1 voltage = ± 200 kV). Various conditions in terms of the hit rates on the Defining counter were realized by changing the IF-V slit width. We obtained the data with hit rates from 40 kilo to 1.4 mega hits per spill.

In addition to the beam rate study, we narrowed the $\overline{HighTh}$ veto widths for the study of pileup with FADC data in the condition #9, 12, 13, and changed beam direction on purpose to directly hit on the SDD for the study of the background origin in the condition #6, 7. These data were not analyzed in this thesis.

The recorded data for each event are listed in Table 5.4 and a data summary for each condition is described in Table 5.5. Scaler values of each SDD discriminator for each condition are plotted in Fig 5.9.

Table 5.4: Obtained data in the beam commissioning.

	module	remark
	TKO PHADC	Signal Hight
OUT (3.0 μs)	VME PHADC	Signal Hight
	VME FADC	Wave form analysis
FOUT	TKO PHADC	Correlation cut with OUT
XOUT	TKO PHADC	Baseline information
OUT (0.2 μs)	TKO TDC	SDDOR start
	TKO TDC	T0 start
Reset Timing	TKO TDC	SDDOR start
HighTh Timing	TKO TDC	SDDOR start
Define Timing	TKO TDC	SDDOR start
T0 Timing	TKO TDC	SDDOR start
First level Timing	TKO TDC	SDDOR start, identify $SDDself$ trigger
beamline counters	TKO	PID by TOF etc...
beamline chambers	TKO	track information
Scaler counts	VME	LowTh, HighTh, Reset, DAQ info etc...

Table 5.5: Data summary of the SDD beam commissioning.

Date	Beam intencity	Duration (hours)	Define rate (k/spill)	Yield (k counts) Ti K_α	Ni K_α	remark	condition #
Nov.	2.9 kW	2.9	443	13.5	21.1		1
8		2.9	100	2.6	3.6		2
Nov.	3.15 kW	2.1	399	7.8	11.3		3
8∼9		2.8	106	2.1	4.5		4
		0.7	1006	5.3	9.5	SDDself only	5
		0.6	495	3.5	2.3	D5 +45 (direct hit)	6
		0.6	303	2.2	2.0	D5 -60 (direct hit)	7
Nov.	3.55 kW	1.2	427	4.6	6.7		8
9∼10		1.0	423	3.9	5.8	$\overline{HighTh}$ width 1/10	9
		1.8	47	0.9	1.2		10
		2.9	431	11.8	16.8		11
		0.4	1434	3.9	7.3	SDDself only $\overline{HighTh}$ width 1/10	12
		0.4	1434	3.5	7.0	SDDself only $\overline{HighTh}$ width 1/100	13

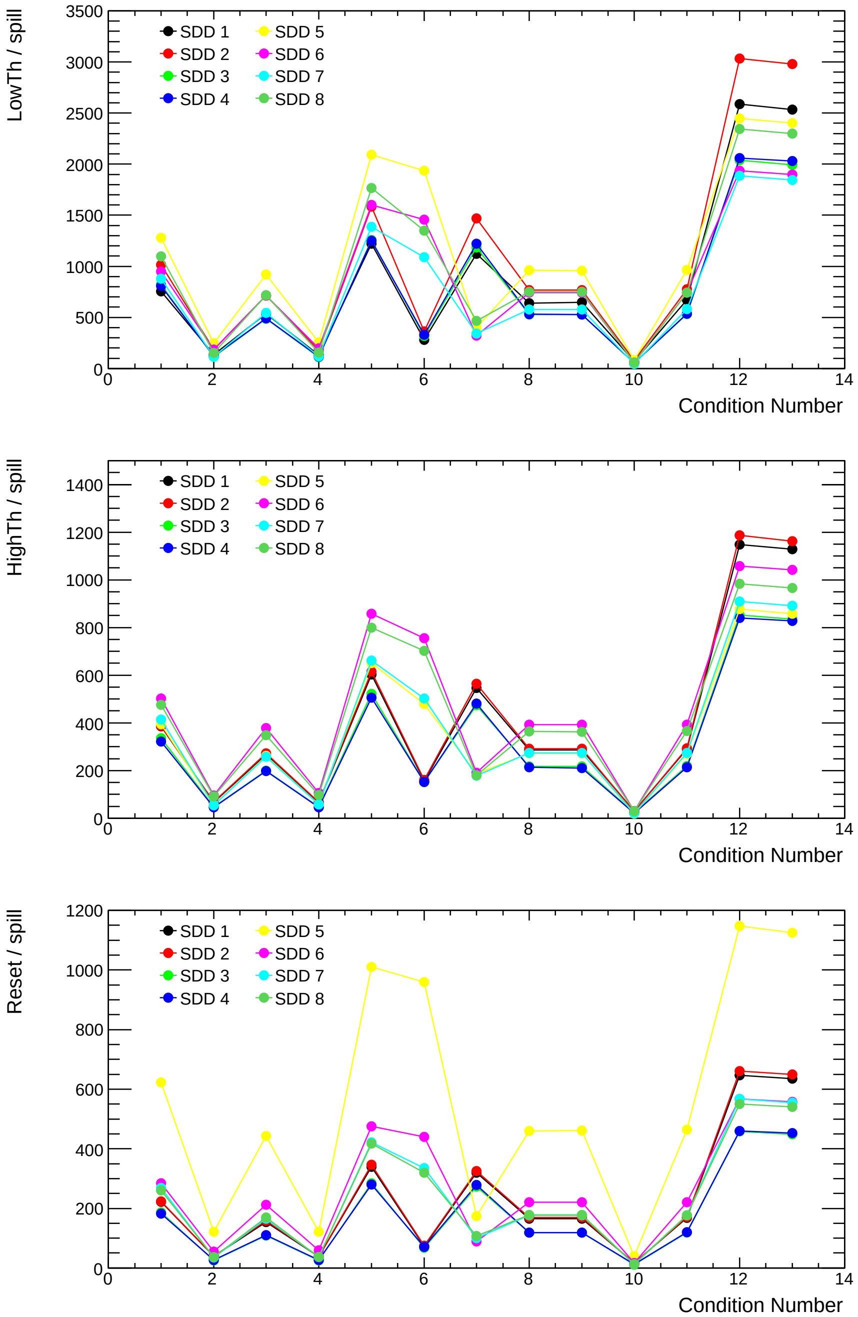

Figure 5.9: Scaler counts of each discriminator for each SDD.

5.4 Analysis

5.4.1 Cut Condition

To reduce the pileup events, cross-talk events and other irregular signals, we applied following cuts for all the data.

- Single hit event selection
- Baseline cut by 3 Gaussian σ
- OUT-FOUT correlation cut
- Reset-followed event cut
- HighTh-followed event cut

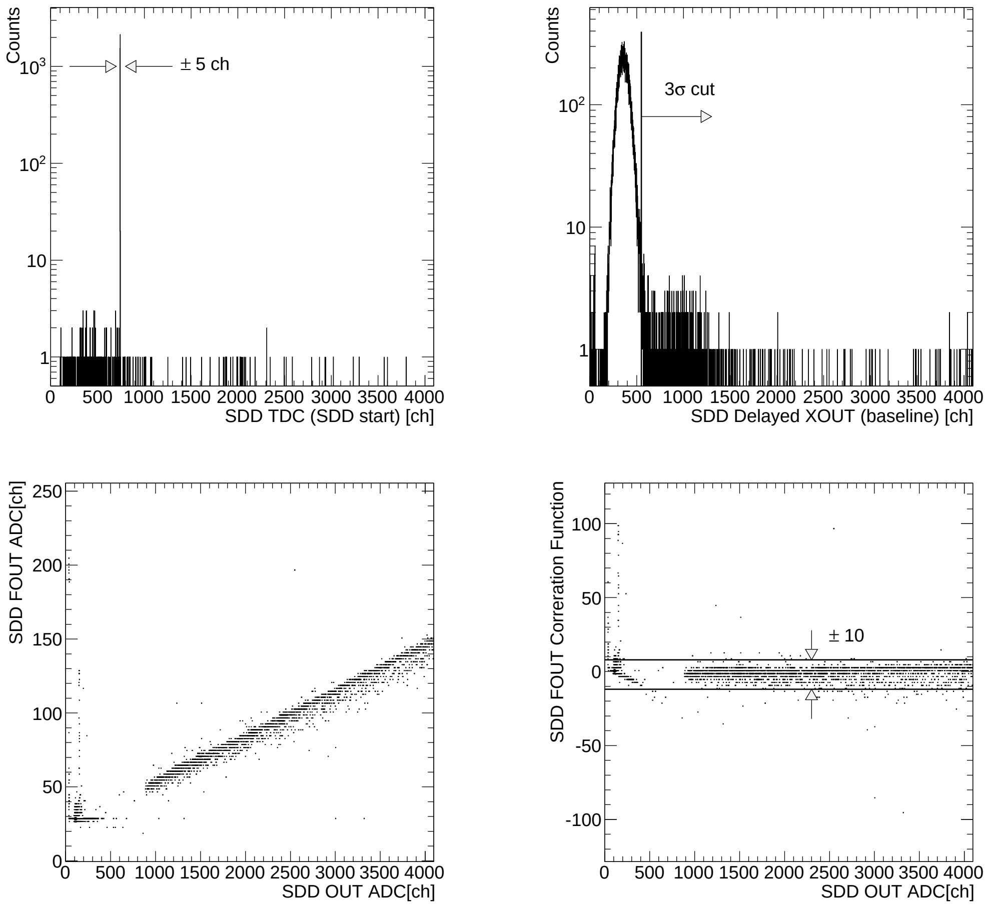

Figure 5.10: Common cut conditions. (a) select the events which made the triggers, (b) baseline cut, (c) OUT-FOUT correlation, (d) OUT-FOUT correlation cut.

5.4.2 Spectral Fitting

After applying the common cut conditions, gains of 8 SDDs were roughly adjusted. Then summed up spectra of 8 SDDs were studied.

First, we checked the typical energy resolution in the beam commissioning. A summed spectrum of condition #3 was fitted by response functions for 6 x-ray lines and a second order polynomial background. As for response functions, only *Gauss* and *Tail* components were included.

The spectrum and the result of the fitting is shown in Fig. 5.11 and Fig. 5.12. The resolution at Kaonic ^{3}He L_α energy was estimated to be better than 150 eV from the obtained resolutions of 3 K_α peaks. Thus, a successful operation of all 8 SDDs in a realistic beam condition was confirmed. However, the peak position of the Fe K_α could not be correctly reproduced from the titanium and nickel peaks so far.

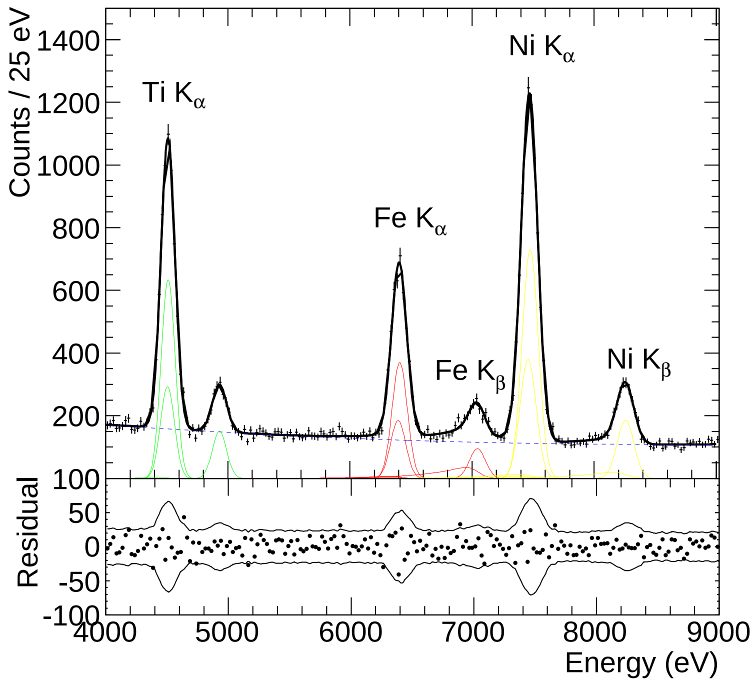

Figure 5.11: Typical spectrum in the beam commissioning (condition #3). χ^2/ndf = 161.2/176.

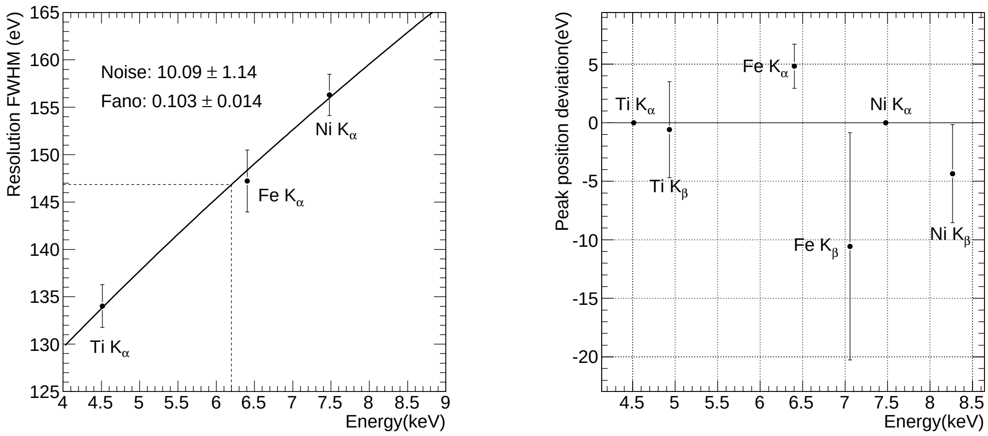

Figure 5.12: (a) Energy resolutions obtained in the fitting. (b) Energy deviations from the energy scale calibrated by Ti and Ni $K_{\alpha1}$ peaks.

5.4.3 Characteristic X-ray Yields

Then we tried fittings for each condition to see the difference of the characteristic x-ray yields and the signal-to-noise ratio. In these fittings we used only *Gauss* for the response functions.

The yields were defined by the Gaussian area. Figure 5.13 shows the yields dependence on the beam rate. Condition # 1, 2, 3, 4, 5, 8, 10 and 11 were plotted here since the conditions of these runs differ only in the hit rate on the Defining counter controlled by the opening width of IF-V slit.

We can see linear dependences of the x-ray yields on the beam rate as naively expected. From the linear fitting of these points, the yields are evaluated to be

- $\sim$900 Ti K_α / hour / 100 k beam on the Defining counter
- $\sim$1400 Ni K_α / hour / 100 k beam on the Defining counter

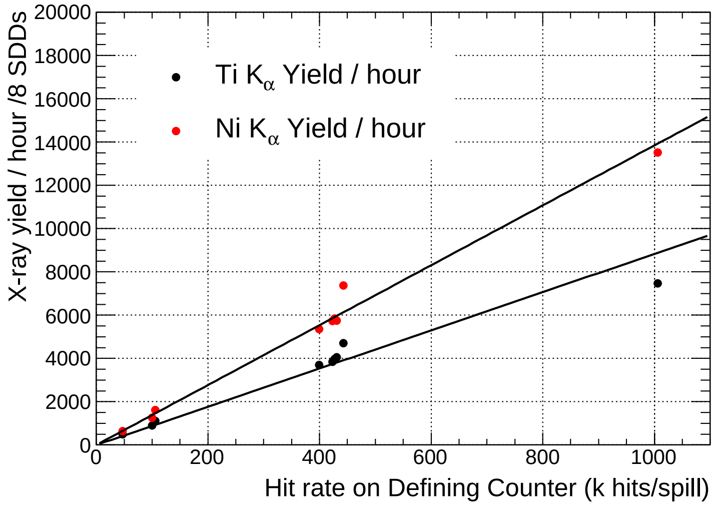

Figure 5.13: Characteristic x-ray yields at the different beam rates.

5.4.4 Signal to Noise Ratio

Without a calculation, we could see the improvement of the signal-to-noise ratio in calibration spectrum compared to E570 (Figure 5.14). It may due to the improvement of the K/π ratio of the beam or the detector geometry. However, we can not directly compare to the E570 result since we had not installed the degrader and the target in the commissioning. In-flight reactions with them are expected to increase high-energy γ-ray background.

As for the rate dependency, we only observed a small difference for the wide range of the beam rate (Figure 5.15). Here we defined the signal-to-noise ratio as

$$SN = \frac{\mathrm{TiK}_\alpha Gauss\, Gain}{\int_{\mathrm{TiK}_\alpha^{\mathrm{mean}}-\mathrm{TiK}_\alpha^{\mathrm{FWHM}}}^{\mathrm{TiK}_\alpha^{\mathrm{mean}}+\mathrm{TiK}_\alpha^{\mathrm{FWHM}}} \mathrm{pol1(E)\ dE}} \tag{5.1}$$

But it does not mean the same holds for the “kaonic x-ray spectrum”, whose signal-to-noise ratio is expected to have strong dependence on the stopped-K^-/other particles ratio of the beam.

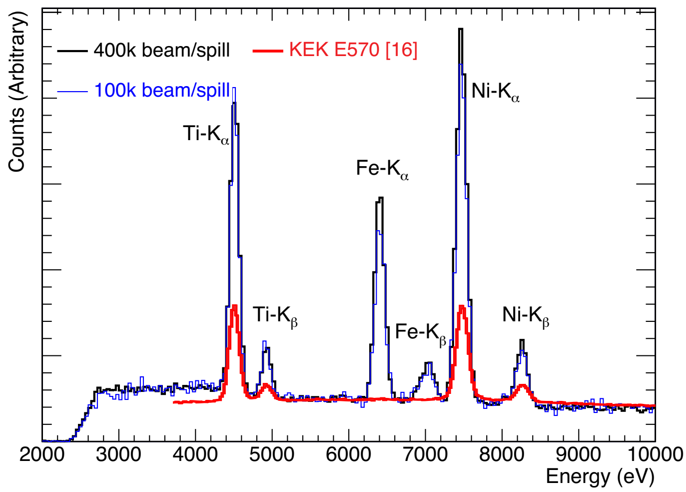

Figure 5.14: Comparison with the E570 calibration spectrum.

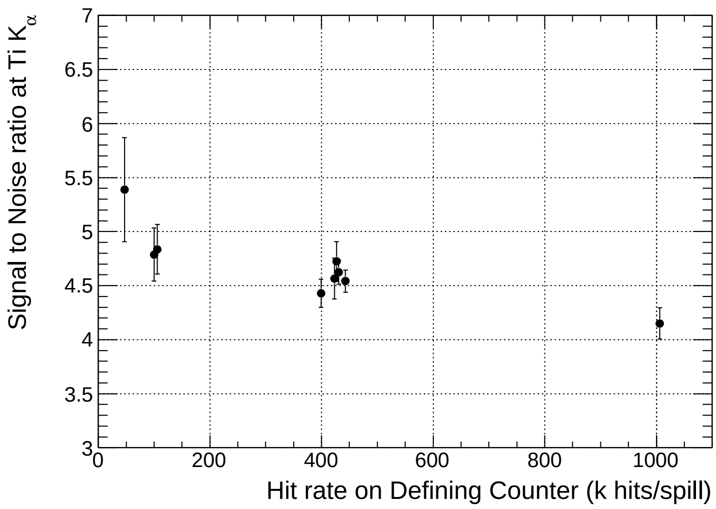

Figure 5.15: Signal-to-noise ratio at the different beam rates.

Chapter 6

Conclusion

First, we searched the optimal operational condition within the experimental requirements; SDDs at low temperatures and their preamplifiers also in the vacuum. After optimizing the bias voltages, the temperature behaviors were investigated in terms of the energy resolution, time resolution, and the dead time. We found 130 K and over 270 K were optimal for the SDDs and preamplifiers, respectively, in which condition the energy resolution at 6 keV was $\sim$ 150 eV in FWHM and the time resolution was $\sim$ 500 ns in FWHM.

Next, we succeeded in rejecting pileup events caused by the charged particle hits, which will significantly contribute to reduce the systematic error in E17 and enabled us to study further systematic effect on the response function of the SDD. Although we found no dependence of the response function on the detection rate, there was a significant dependence on the incident angle. It should be properly considered in E17 since the incident-angle distributions are completely different for the kaonic helium x-rays and the characteristic x-rays for the energy calibration.

Then, the validity of the energy scale calibrated by the characteristic x-rays of titanium and nickel was studied. The Mn K_α energy was reproduced with a deviation below 1 eV from the reference value including the incident-angle effect.

Finally, we performed the commissioning with the beam. All 8 SDDs were worked properly with a good energy resolution ($<$ 150 eV in FWHM at 6 keV). The beam commissioning also revealed that the background level was smaller than KEK E570. However it may partly due to the absence of the degrader and the target.

Toward the physics data taking, which is expected to be performed in JFY

2011, we need further studies in the final setup especially on the linearity of the energy scale and the longterm stability.

Acknowledgement

First of all, I would like to express my sincere gratitude to my supervisor, Prof. R. S. Hayano, who introduced me this interesting field of physics. He gave me continuous support and valuable advice throughout my work and learning in these two years.

I am grateful to Dr. H. Outa and Dr. T. Suzuki, under whom I started my experimental carrier with beamline works. Their great knowledge about the experimental techniques always impressed me and I learned a lot from them.

I would like to thank Dr. M. Sato and Dr. M. Iio with sincere respect. We have always worked together at Tsukuba and Tokai. Dr. M. Sato taught me how to deal the x-ray detectors, and also the researching attitude and procedure with deeds as well as words. This work owes so much to them. Dr. M. Iio taught me many things about the cryogenic physics and often encouraged me with the warmest words.

I am grateful to Dr. S. Ishimoto, who helped us as a cryogenic specialist. He also kindly took us to lunch so many times at Tsukuba.

I also acknowledge Prof. E. Widmann, Dr. J. Zmeskal, Dr. T. Ishiwatari and Ms. B. K. Wunschek, who arranged the x-ray detectors and sometimes joined the work at Japan.

I would like to express my best regards to all the other collaborators of J-PARC E17 experiment for their helps and advices. I hope that our powerful collaboration will end up with a great success of the experiment.

Lastly, I would like to express my gratitude to all the people who supported and encouraged me, including the members of the nuclear experiment group at Hongo, my friends and my family.

Appendix

Appendix A

Asymmetry in Characteristic X-ray Lines

Since we calibrate the energy scale by using Ni and Ti K_α lines, the effect of the natural line shapes of them to the resulting peak positions in the fitting is of great interest.

Asymmetry due to the satellite lines

K_α x-rays are emitted when a K shell vacancy is filled with a L shell electron (2p $\rightarrow$ 1s), and the fine structure due to the spin-obit coupling separates them to two lines ($K_{\alpha 1}$: $2p_{\frac{3}{2}} \rightarrow 1s$, $K_{\alpha 2}$: $2p_{\frac{1}{2}} \rightarrow 1s$). Furthermore, the real spectra have much more satellite multiplets due to the additional vacancies in the outer shell, which make the peak shape asymmetric. As for the K_α lines of 3d transition metals, the peak shapes can be approximated by using 5 or 6 Lorentzian peaks as shown in Fig. A.1 and Fig. A.2 [28, 29].

In our measurements, Ti and Ni K_α lines were considered to be suffered from such effect since they were induced by the electrons which could create additional vacancies in the outer shell. On the other hand, Mn K_α line which came from the ^{55}Fe source were considered to be simply represented by the summation of two symmetric lines.

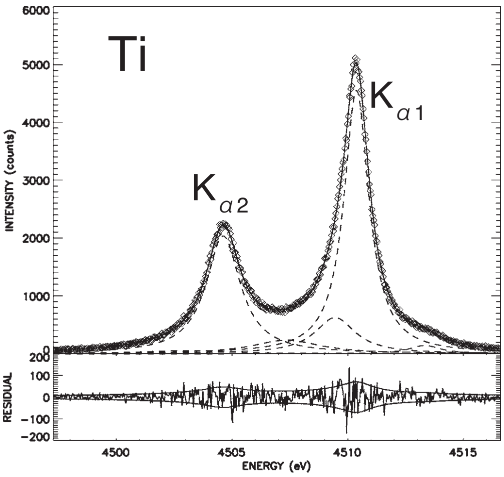

Figure A.1: Measured Ti K_α line shape [28].

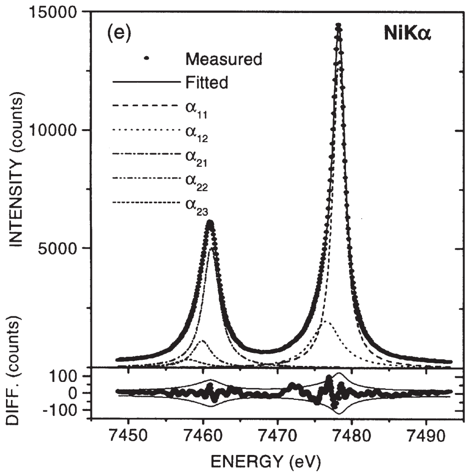

Figure A.2: Measured Ni K_α line shape [29].

Effect to the fitting result [30]

We generated K_α lines with satellite lines like Fig. A.3 and smeared it with the SDD energy resolution as shown in Fig. A.4. The parameters used to generate the original line shape are listed in Table A.1. Then the smeared spectra were fitted with asymmetric and symmetric Gaussians, where the symmetric Gaussian was the summation of the two Gaussians with the mean value of $K_{\alpha 1}$ and $K_{\alpha 2}$, and the asymmetric one was the summation of 5 or 6 Gaussians with the mean values given in Table A.1. Intensity ratios for the each Gaussian were fixed.

The resulting energy deviations are plotted in Fig. A.5, where the energy deviation ΔE is defined by

$$\Delta E = E_{fit} - E_{org}.$$

E_{fit} and E_{org} are the values obtained in the fitting and the energy originally used to generate the spectrum.

Considering that the Mn K_α can be represented by the asymmetric Gaussian, our study indicates Mn K_α energy become $\sim$ 0.3 eV larger when we calibrated the energy scale by using asymmetric Gaussian for Ti and Ni peaks. Thus, the asymmetric Gaussians should be used for the Ti and Ni fluorescence x-ray peaks.

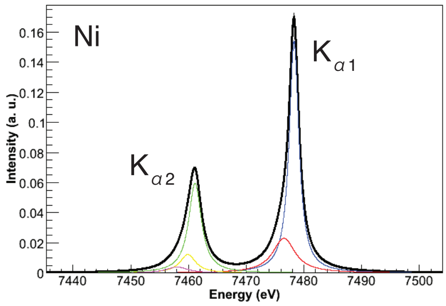

Figure A.3: Generated line shape of Ni K_α with satellite peaks.

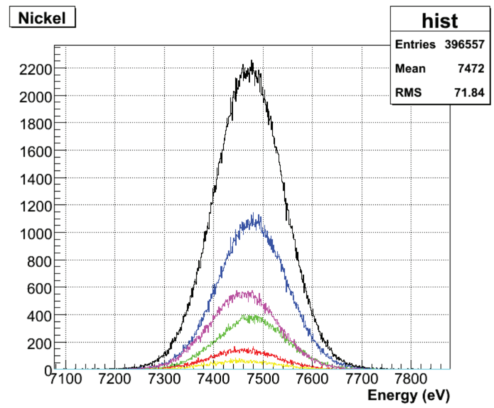

Figure A.4: The generated spectrum was smeared by the detector resolution.

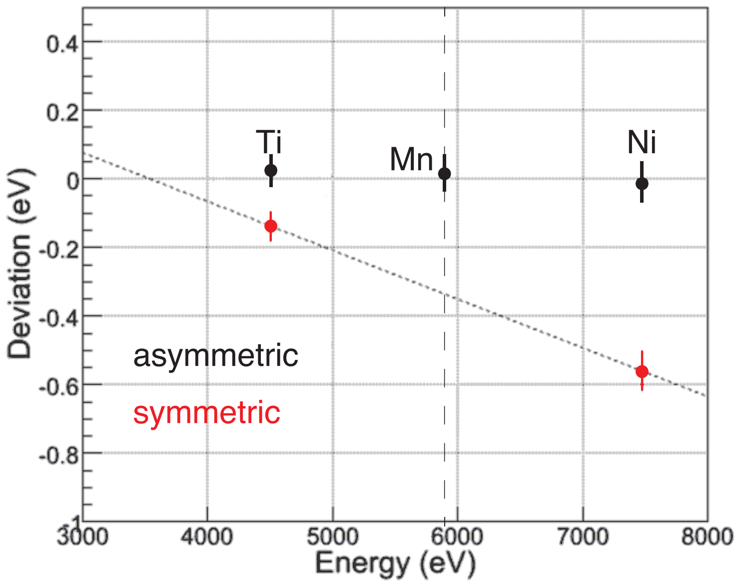

Figure A.5: Energy deviations between the fitting results and the values used to generate the spectra.

Table A.1: Parameters used to generate the spectrum with satellite lines.

Element	peak	mean(eV)	width (eV)	Intensity (a.u)	Reference
Ti	α_{11}	4510.901	1.36	236480	[28]
	α_{12}	4509.940	2.21	51208	
	α_{13}	4507.757	3.74	31099	
	α_{15}	4513.975	1.70	8831	
	α_{21}	4504.911	1.88	143370	
	α_{21}	4503.092	4.48	8073	
Ni	α_{11}	7478.281	2.013	0.487	[29]
	α_{12}	7476.529	4.711	0.171	
	α_{21}	7461.131	2.674	0.250	
	α_{22}	7459.874	3.039	0.064	
	α_{23}	7458.029	4.476	0.028	

Bibliography

[1] C. J. Batty, E. Friedman, A. Gal, Physics Reports 287 (1997) 385 – 445.

[2] C. Wiegand, R. Pehl, Phys. Rev. Lett. 27 (1971) 1410–1412.

[3] C. Batty, S. Biagi, S. Hoath, J. Sharman, Nuclear Physics A 326 (1979) 455–462.

[4] S. Baird, C. Batty, F. Russell, P. Sharman, P. Bird, A. Clough, K. Parker, G. Pyle, G. Squier, Nuclear Physics A 392 (1983) 297–310.

[5] J. Batty, Nuclear Physics A 508 (1990) 89c.

[6] S. Hirenzaki, Y. Okumura, H. Toki, E. Oset, A. Ramos, Physical Review C 61 (5) (2000) 055205.

[7] R. Seki, Physical Review C 5 (1972) 1196.

[8] J. Koch, M. Sternheim, Physical Review C 5 (1972) 381.

[9] A. Kudrjavtsev, V. Mur, V. Popov, Physics Letters B 143 (1984) 41.

[10] S. Wycech, Nuclear Physics A 450 (1986) 399c–402c.

[11] M. Iwasaki, R. S. Hayano, T. M. Ito, S. N. Nakamura, T. P. Terada, D. R. Gill, L. Lee, A. Olin, M. Salomon, S. Yen, K. Bartlett, G. A. Beer, G. Mason, G. Trayling, H. Outa, T. Taniguchi, Y. Yamashita, R. Seki, Physical Review Letters 78 (1997) 3067–3069.

[12] Y. Akaishi, T. Yamazaki, Physical Review C 65 (2002) 044005.

[13] Y. Akaishi, Proceedings for International Conference on Exotic Atoms and Related Topics (EXA05) (2005) 45.
URL `http://dx.doi.org/10.1553/exa05s45`

[14] S. Okada, G. Beer, H. Bhang, M. Cargnelli, J. Chiba, Physics Letters B 653 (2007) 387–391.

[15] M. Bazzi, G. Beer, L. Bombelli, A. Bragadireanu, M. Cargnelli, G. Corradi, C. C. Petrascu, A. d'Uffizi, C. Fiorini, T. Frizzi, F. Ghio, B. Girolami, C. Guaraldo, R. Hayano, M. Iliescu, T. Ishiwatari, M. Iwasaki, P. Kienle, P. L. Sandri, A. Longoni, V. Lucherini, J. Marton, S. Okada, D. Pietreanu, T. Ponta, A. Rizzo, A. R. Vidal, A. Scordo, H. Shi, D. Sirghi, F. Sirghi, H. Tatsuno, A. Tudorache, V. Tudorache, O. V. Doce, E. Widmann, J. Zmeskal, Physics Letters B 681 (2009) 310 – 314.

[16] M. Bazzi, G. Beer, L. Bombelli, A. M. Bragadireanu, M. Cargnelli, G. Corradi, C. Curceanu, A. d'Uffzi, C. Fiorini, T. Frizzi, F. Ghio, B. Girolami, C. Guaraldo, R. S. Hayano, M. Iliescu, T. Ishiwatari, M. Iwasaki, P. Kienle, P. L. Sandri, A. Longoni, J. Marton, S. Okada, D. Pietreanu, T. Ponta, A. Rizzo, A. R. Vidal, A. Scordo, H. Shi, D. L. Sirghi, F. Sirghi, H. Tatsuno, A. Tudorache, V. Tudorache, O. V. Doce, E. Widmann, J. Zmeskal, arXiv nucl-ex 1010.4631.

[17] R. S. Hayano, et al., Proposal for J-PARC 50 GeV Proton Synchrotron.

[18] E. Gatti, P. Rehak, Nuclear Instruments and Methods in Physisc Research A 225 (1984) 608–614.

[19] P. Lechner, C. Fiorini, R. Hartmann, J. Kemmer, N. Krause, P. Leutenegger, A. Longoni, H. Soltau, D. Stter, R. Stter, L. Strer, U. Weber, Nuclear Instruments and Methods in Physisc Research A 458 (2001) 281 – 287.

[20] KETEK.
URL `http://www.ketek.net`

[21] G. Beer, A. M. Bragadireanu, M. Cargnelli, C. Curceanu-Petrascu, J.-P. Egger, H. Fuhrmann, C. Guaraldo, M. Iliescu, T. Ishiwatari, K. Itahashi, M. Iwasaki, P. Kienle, T. Koike, B. Lauss, V. Lucherini, L. Ludhova, J. Marton, F. Mulhauser, T. Ponta, L. A. Schaller, R. Seki, D. L. Sirghi, F. Sirghi, J. Zmeskal, Physical Review Letters 94 (21) (2005) 212302.

[22] M. Bazzi, G. Beer, L. Bombelli, A. Bragadireanu, M. Cargnelli, G. Corradi, C. C. Petrascu, A. d'Uffizi, C. Fiorini, T. Frizzi, Nuclear Instruments and Methods in Physisc Research A in print.

[23] Canberra.
URL `http://www.canberra.com/`

[24] National institute of standards and technology, X-ray Transition Energy Database.
URL `http://www.nist.gov/pml/data/xraytrans/index.cfm`

[25] C. Canali, C. Jacoboni, F. Nava, G. Ottaviani, A. Alberigi-Quaranta, Physical Review B 12 (1975) 2265–2284.

[26] M. Mazziotta, Nuclear Instruments and Methods in Physisc Research A 584 (2008) 436 – 439.

[27] J. L. Campbell, L. McDonald, T. Hopman, T. Papp, X-Ray Spectrometry 30 (2001) 230–241.

[28] C. T. Chantler, M. N. Kinnane, C.-H. Su, J. A. Kimpton, Physical Review A 73 (2006) 012508.

[29] G. Hölzer, M. Fritsch, M. Deutsch, J. Härtwig, E. Förster, Physical Review A 56 (1997) 4554–4568.

[30] M. Sato, internal report.